Utilizing machine learning algorithm and Carrera unified formulation for vibration analysis of nanocomposite-enhanced bridge structures rested on an innovative elastic foundation: verification of the results via nondestructive testing

Wenjie Yang, Gongxing Yan, Khalid A. Alnowibet & Mohammed El-Meligy

Published online: 17 Oct 2024.

Submit your article to this journal ⎘

View related articles ⎘

View Crossmark data ⎘

Taylor & Francis
Taylor & Francis Group

Check for updates

ORIGINAL ARTICLE

Utilizing machine learning algorithm and Carrera unified formulation for vibration analysis of nanocomposite-enhanced bridge structures rested on an innovative elastic foundation: verification of the results via nondestructive testing

Wenjie Yang[a,b], Gongxing Yan[c,d], Khalid A. Alnowibet[e], and Mohammed El-Meligy[f,g]

[a]School of Materials Science and Engineering, Wuhan Institute of Technology, Wuhan, China; [b]Sichuan Jinghengxin Construction Engineering Testing Co., Ltd, Luzhou, China; [c]School of Intelligent Construction, Luzhou Vocational and Technical College, Luzhou, China; [d]Luzhou Key Laboratory of Intelligent Construction and Low-Carbon Technology, Luzhou, China; [e]Statistics and Operations Research Department, College of Science, King Saud University, Riyadh, Kingdom of Saudi Arabia; [f]Jadara University Research Center, Jadara University, Jordan; [g]Applied Science Research Center, Applied Science Private University, Amman, Jordan

ABSTRACT

This paper presents an advanced vibration analysis of Al_2O_3 nanocomposite-reinforced concrete bridge structures resting on an innovative elastic foundation using the Carrera Unified Formulation (CUF). The primary objective is to investigate the dynamic response of these bridges under various loading conditions, accounting for the reinforcing effects of Al_2O_3 nanocomposites within the concrete matrix. The formulation incorporates a novel elastic foundation model designed to more accurately simulate realistic boundary conditions and soil-structure interaction. The accuracy and reliability of the CUF-based vibration analysis are further validated using nondestructive testing (NDT) techniques, which enable the detection of potential damage and anomalies in the bridge structures. Moreover, a machine learning (ML) algorithm is employed to predict the vibrational characteristics, facilitating an efficient comparison with the results obtained from CUF and NDT. The combination of theoretical modeling, experimental verification, and ML predictions highlights the robustness of the proposed method. The results demonstrate the effectiveness of using Al_2O_3 nanocomposites to enhance the mechanical properties of bridge structures, improving their vibrational performance, stability, and longevity. This study provides a comprehensive framework for future applications in bridge engineering, combining high-fidelity numerical methods with state-of-the-art testing and computational techniques.

1. Introduction

Composite structures have become increasingly important for engineers due to their ability to combine materials with distinct properties, resulting in structures with superior performance [1–3]. These materials offer enhanced strength-to-weight ratios, allowing engineers to design lighter yet stronger structures, which is particularly beneficial in industries like aerospace, automotive, and civil engineering [4, 5]. In aerospace engineering, composite materials have revolutionized aircraft design, reducing weight and fuel consumption while maintaining structural integrity under high stresses [6, 7]. The lightweight nature of composites allows for greater efficiency and payload capacity without compromising safety [8, 9]. In civil engineering, composite structures are used to strengthen and reinforce bridges, buildings, and infrastructure [10, 11, 12]. They provide higher durability, resistance to corrosion, and reduced maintenance costs compared to traditional materials like steel and concrete [13, 14]. Composite materials also offer engineers the ability to tailor material properties to specific applications. By adjusting the type, orientation, and

volume of reinforcement (e.g. fibers, particles), engineers can create structures that meet precise performance requirements, such as improved thermal insulation, electrical conductivity, or impact resistance [15–17]. The flexibility in design also allows for more complex shapes and geometries, which are difficult to achieve with conventional materials. This enables innovative architectural designs and structures with optimized aerodynamics or load-bearing capacities. Furthermore, composite structures exhibit excellent fatigue resistance, making them ideal for applications subjected to repetitive loading, such as wind turbines, marine structures, and sports equipment [18]. Engineers also benefit from the sustainability of composites, as many composite materials can be made from recyclable or environmentally friendly components, aligning with the growing demand for eco-conscious engineering solutions [19]. In the automotive industry, composites are being used to improve vehicle performance by reducing weight, increasing fuel efficiency, and enhancing crash safety through energy absorption [20, 21]. This has led to the development of safer, greener vehicles. Composites are also essential for

---

CONTACT Gongxing Yan ✉ yaaangx@126.com School of Intelligent Construction, Luzhou Vocational and Technical College, Luzhou, China.

engineers working in the renewable energy sector, where lightweight, strong materials are needed to construct large-scale structures like wind turbine blades, which must withstand harsh environmental conditions over long periods [22]. The corrosion resistance of composites makes them particularly valuable for structures exposed to aggressive environments, such as offshore platforms, pipelines, and chemical plants (23). This leads to extended service life and lower life-cycle costs [23]. Additionally, composite structures are highly customizable, allowing engineers to integrate multiple functionalities into a single structure, such as combining structural support with thermal or acoustic insulation [24, 25]. Overall, the versatility, durability, and high performance of composite structures have made them a cornerstone of modern engineering, enabling innovation across numerous industries while enhancing efficiency, safety, and sustainability [26, 27].

The CUF is a vital tool for modeling structures and systems due to its ability to unify various structural theories within a single framework. It enables the analysis of beams, plates, and complex three-dimensional structures with high accuracy and efficiency [28]. One of its key advantages is the capability to model both simple and advanced structures without requiring multiple formulations, streamlining the analysis process [29]. CUF provides accurate predictions of mechanical behavior, including stresses and deformations, especially in thick, multilayered, and composite structures [30]. Its multiscale modeling capabilities allow it to address problems ranging from nano- to macro-scales, making it highly versatile. The formulation is also extendable to handle multiphysics phenomena, such as fluid-structure interaction and thermal effects, broadening its application scope [31]. Furthermore, CUF is computationally efficient, enabling engineers to select appropriate levels of refinement for different applications without sacrificing precision [30]. It plays a critical role in industries like aerospace and civil engineering, where it helps optimize material usage and enhance structural performance [25]. CUF's precision makes it an excellent tool for structural health monitoring, as it accurately simulates real-world conditions and helps detect potential damage early. Overall, CUF has become an essential framework in both academic research and industrial applications, offering unparalleled flexibility and reliability [32].

Constitutive models play a critical role in engineering, as they provide mathematical descriptions of how materials respond to various loading conditions [33, 34]. For engineers, understanding material behavior under different stresses, strains, and environmental conditions is essential for designing safe and reliable structures [35, 36]. A well-defined constitutive model allows engineers to predict material responses, such as deformation, failure, or fatigue, under both normal and extreme conditions [37, 38]. In structural engineering, for example, constitutive models help simulate the mechanical behavior of materials used in buildings, bridges, and other infrastructure [39, 40]. These models enable engineers to anticipate how materials like steel, concrete, or composites will behave over time, accounting for factors such as temperature changes, loading cycles, and aging [41, 42]. Without accurate models, structural failures

could occur, leading to catastrophic consequences [43, 44]. For civil engineers, constitutive models are crucial in assessing soil behavior and stability [45, 46]. Soil is a complex material, exhibiting nonlinear, time-dependent responses that vary with moisture content, stress history, and other factors [20, 47]. Using constitutive models, engineers can evaluate soil performance during construction, preventing issues like foundation settlement or slope failure [21, 48]. In aerospace engineering, constitutive models are essential for predicting how advanced materials, such as composites, perform under high stresses and temperatures [49, 50]. Engineers rely on these models to design lighter, stronger aircraft that can withstand the demands of flight while ensuring safety and durability [51, 52]. Moreover, in biomechanics, constitutive models help engineers understand the mechanical behavior of biological tissues [53, 54]. This knowledge is vital for designing medical devices, prosthetics, and implants that interact safely and effectively with the human body [55]. Engineers working on energy infrastructure, such as pipelines or offshore platforms, also depend on constitutive models to predict material behavior under harsh environmental conditions [56, 57]. This ensures that materials can withstand factors like corrosion, pressure, and temperature fluctuations [58]. The importance of constitutive models extends to manufacturing processes as well [59]. Engineers use these models to simulate processes such as metal forming, welding, and additive manufacturing, optimizing the performance of materials and reducing production costs [60]. Furthermore, constitutive models assist engineers in assessing the long-term performance and durability of materials [61].

Using the Carrera Unified Formulation, an enhanced vibration analysis of Al_2O_3 nanocomposite-reinforced concrete bridge structures resting on a novel elastic foundation is presented in this research. The main goal is to look into how these bridges respond dynamically to different loading scenarios while taking the reinforcing effects of Al_2O_3 nanocomposites in the concrete matrix into consideration. In order to more realistically mimic boundary conditions and soil-structure interaction, a unique elastic foundation model has been included in the formulation. Nondestructive testing methods are used to further confirm the accuracy and reliability of the CUF-based vibration analysis. NDT techniques allow for the identification of possible damage and abnormalities in the bridge structures. In addition, a machine learning method is used to forecast the vibrational properties, allowing for a more effective comparison with the CUF and NDT findings. The robustness of the suggested approach is highlighted by the integration of ML predictions, experimental verification, and theoretical modeling. The results show how well Al_2O_3 nanocomposites work to improve the mechanical characteristics of bridge structures, resulting in increased stability, lifespan, and vibrational performance. This work offers a thorough framework that combines cutting-edge testing and computational approaches with high-fidelity numerical methods for future applications in bridge engineering.

2. Mathematical modeling

2.1. Material properties of the metal layer reinforced by concrete–Al$_2$O$_3$ nanocomposites

Based on a modified model that takes into consideration the rule of mixing and the micromechanical model created by Shaat et al. [62], which accounts for the impact of grain boundary size, the elastic modulus of the fabricated materials was calculated analytically. This work established a modified model that takes into account the effects of grain refinement, grain boundary size, and the volume percentage of reinforcement that has not been developed previously. Using the law of mixing, the produced nanocomposite's mechanical characteristics may be stated as follows:

$$E_{com} = E_m V_m + E_c V_c \tag{1a}$$

$$\rho_{com} = \rho_m V_m + \rho_c V_c \tag{1b}$$

$$\nu_{com} = \nu_m V_m + \nu_c V_c \tag{1c}$$

where the elastic moduli of the ceramic, matrix, and composite are denoted by the letters E_{com}, E_m, and E_c, respectively. The volume fractions of the ceramic and matrix are denoted by V_c and V_m, respectively. However, it may be calculated using the Shaat et al. [62] micromechanical model as follows:

$$E_{com} = E_m \frac{\rho_1 \mathcal{T}_g^2 + \rho_2 \mathcal{T}_g + \rho_3}{\mathfrak{I}_1 \mathcal{T}_g^2 + \mathfrak{I}_2 \mathcal{T}_g + \mathfrak{I}_3} \tag{2}$$

where the parameters $\rho_1, \rho_2, \rho_3, \mathfrak{I}_1, \mathfrak{I}_2$ and $\mathfrak{I}_3$ are determined by the ratio between the matrix elastic modulus and the grain boundary. The parameter $\mathcal{T}_g$ regulates the proportion of grain size to grain border size, as stated in Mohamed [63]:

$$\rho_1 = -20\mathfrak{Y}(\mathfrak{Y} - 1)^2 \left(\nu - \frac{7}{5}\right)\left(\nu - \frac{1}{2}\right), \tag{3a}$$

$$\rho_2 = -20\mathfrak{Y}\left((-\mathfrak{Y} - 2)\nu + \frac{7\mathfrak{Y}}{5} + \frac{8}{5}\right)(\mathfrak{Y} - 1)\left(\nu - \frac{1}{2}\right)$$
$$- 20\mathfrak{Y}\left(\nu - \frac{7}{5}\right)(\mathfrak{Y} - 1)\left(\left(-\mathfrak{Y} + \frac{1}{4}\right)\nu + \frac{\mathfrak{Y}}{2} + \frac{1}{4}\right) \tag{3b}$$

$$\rho_3 = -20\mathfrak{Y}\left((-\mathfrak{Y} - 2)\nu + \frac{7\mathfrak{Y}}{5} + \frac{8}{5}\right)\left(\left(-\mathfrak{Y} + \frac{1}{4}\right)\nu + \frac{\mathfrak{Y}}{2} + \frac{1}{4}\right), \tag{3c}$$

$$\xi_1 = 30(1 + \nu)(\mathfrak{Y} - 1)^2 \left(\nu - \frac{1}{2}\right)\left(\nu - \frac{13}{15}\right), \tag{3d}$$

$$\xi_2 = -30(\mathfrak{Y} - 1)\left(-\frac{1}{5} + \nu\right)$$
$$\left((\mathfrak{Y} - 1)\nu^2 + \left(-\frac{5\mathfrak{Y}}{6} - \frac{1}{6}\right)\nu + \frac{\mathfrak{Y}}{6} + \frac{5}{6}\right), \tag{3e}$$

$$\xi_3 = -20\left((\mathfrak{Y} + 2)\nu - \frac{7\mathfrak{Y}}{5} - \frac{8}{5}\right)\left(\left(\mathfrak{Y} - \frac{1}{4}\right)\nu - \frac{\mathfrak{Y}}{2} - \frac{1}{4}\right). \tag{3f}$$

When it is assumed that the sub-grain and the grain border have the same Poisson's ratio, ν. The ratio of the grain boundary's Young's modulus to the sub-grain's is represented by the formula $= E_{gb}/E_0$. The sub-grain volume fraction, or $\mathcal{T}_g$, may be calculated as follows using the crystallite size (D) and grain boundary thickness (t) as inputs:

$$\mathcal{T}_g = \left(\frac{D}{D + 2t}\right)^3 \tag{4}$$

Here, the average size of the sub-grains is expressed using the crystallite size as determined by the XRD studies. The average size of a grain or a dislocation cell is represented by the crystallite size, which is determined by XRD. This is due to the fact that a dislocation cell border or a grain boundary disrupts the coherency of X-ray scattering [64]. ARB-induced high-straining results in a large proportion of sub-grains in the microstructure. As a result, the sub-grain size is represented by the crystallite size as measured by XRD. For an Al$_2$O$_3$ (Alumina)-reinforced composite concrete structure, the mechanical properties such as Young's modulus, Poisson's ratio, and density depend on the proportion of alumina used, the matrix (usually concrete or polymer), and the fabrication process. However, we can provide approximate values based on typical Alumina-reinforced concrete composites:

Young's Modulus (E)

- Concrete (typical): 25 GPa
- Alumina (Al$_2$O$_3$): 350 GPa

Poisson's Ratio (ν)

- Concrete (typical): 0.2
- Alumina (Al$_2$O$_3$): 0.22

Density (ρ)

- Concrete (typical): 2300 kg/m^3
- Alumina (Al$_2$O$_3$): 3950 kg/m^3

3. Basic equations

As previously said, the elastic behavior of the composite shell supported by a novel elastic foundation is investigated in this study with respect to bonding time variation. As shown in Figure 1, the elastic foundation that surrounds the shell construction is sufficiently flexible to include three different kinds of polynomial expansion: sinusoidal, cosinusoidal, and polynomial, each with varying stiffness terms.

4. Carrera unified formulation

4.1. Displacement field assumption

The displacement field and its variation may be extended as a collection of thickness functions and the accompanying
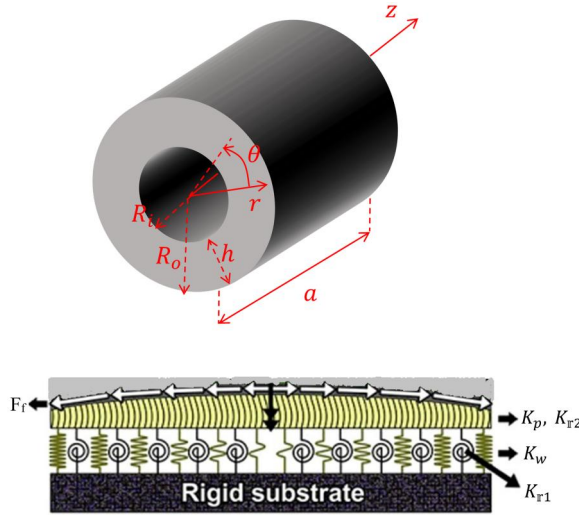
Figure 1. The composite shell's geometry was supported by a novel elastic base.

variables dependent on the in-plane coordinates, according to Carrera's unified formulation. In particular, we have in cylindrical coordinates.

$$\mathbb{u}_\mathbb{r} = f\!\!\!f_\tau(\mathbb{r})\mathbb{u}_{\mathbb{r}\tau}(\theta, \mathbb{z}), \delta\mathbb{u}_\mathbb{r} = f\!\!\!f_s(\mathbb{r})\delta\mathbb{u}_{\mathbb{r}s}(\theta, \mathbb{z})$$
$$\mathbb{u}_\theta = f\!\!\!f_\tau(\mathbb{r})\mathbb{u}_{\theta\tau}(\theta, \mathbb{z}), \delta\mathbb{u}_\mathbb{r} = f\!\!\!f_s(\mathbb{r})\delta\mathbb{u}_{\theta s}(\theta, \mathbb{z}) \quad \tau, s = 0, 1, 2, ..., n$$
$$\mathbb{u}_\mathbb{z} = f\!\!\!f_\tau(\mathbb{r})\mathbb{u}_{\mathbb{z}\tau}(\theta, \mathbb{z}), \delta\mathbb{u}_\mathbb{z} = f\!\!\!f_s(\mathbb{r})\delta\mathbb{u}_{\mathbb{z}s}(\theta, \mathbb{z}) \quad (f\!\!\!f_0 = 1, f\!\!\!f_1 = \mathbb{r}, ..., f\!\!\!f_n = \mathbb{r}^n)$$
(5)

where n indicates the expansion's order, $\mathbb{u}_\mathbb{r}$, $\mathbb{u}_\theta$, and $\mathbb{u}_\mathbb{z}$ are the radial, circumferential, and longitudinal displacements, and $f\!\!\!f_\tau$ is the Taylor expansion function. Repeated indices in Equation (5) and the following denote summation. With the displacement field in cylindrical coordinate $\boldsymbol{\mathcal{U}}^\mathrm{T} = \{\mathbb{u}_\mathbb{r} \quad \mathbb{u}_\theta \quad \mathbb{u}_\mathbb{z}\}$, the compact version of Equation (5) may be expressed as follows.

$$\boldsymbol{\mathcal{U}}(\mathbb{r}, \theta, \mathbb{z}) = f\!\!\!f_\tau(\mathbb{r})\boldsymbol{\mathcal{U}}_\tau(\theta, \mathbb{z}), \delta\boldsymbol{\mathcal{U}}(\mathbb{r}, \theta, \mathbb{z}) = f\!\!\!f_s(\mathbb{r})\delta\boldsymbol{\mathcal{U}}_s(\theta, \mathbb{z})$$
(6)

where $\boldsymbol{\mathcal{U}}_\tau^\mathrm{T} = \{\mathbb{u}_{\mathbb{r}\tau} \quad \mathbb{u}_{\theta\tau} \quad \mathbb{u}_{\mathbb{z}\tau}\}$ and bold letters denote arrays (vectors and matrices). The displacement field at each fundamental nucleus can be approximated using the radial basis shape functions (introduced in Section 4) [65]:

$$\boldsymbol{\mathcal{U}}_\tau(\theta, \mathbb{z}) = \mathfrak{N}_i(\theta, \mathbb{z})\boldsymbol{q}_{\tau i}, \delta\boldsymbol{\mathcal{U}}_s(\theta, \mathbb{z}) = \mathfrak{N}_j(\theta, \mathbb{z})\delta\boldsymbol{q}_{sj} \quad i = 1, 2, ..., n_s$$
(7)

where n_S is the number of nodes in the support domain and $\mathfrak{N}_i$ is the ith shape function. The vector of nodal parameters, or the nucleus displacements at each node in the support domain, is called $q_{\tau i}$, and its variation is called δq_{sj}.

$$\boldsymbol{q}_{\tau i}^\mathrm{T} = \{q_{\mathbb{r}_{\tau i}} \quad q_{\theta_{\tau i}} \quad q_{\mathbb{z}_{\tau i}}\},$$
(8)

Substituting Equation (9) in Equation (8), gives

$$\boldsymbol{\mathcal{U}}(\mathbb{r}, \theta, \mathbb{z}) = f\!\!\!f_\tau(\mathbb{r})\mathfrak{N}_i(\theta, \mathbb{z})\boldsymbol{q}_{\tau i},$$
$$\delta\boldsymbol{\mathcal{U}}(\mathbb{r}, \theta, \mathbb{z}) = f\!\!\!f_s(\mathbb{r})\mathfrak{N}_j(\theta, \mathbb{z})\delta\boldsymbol{q}_{sj}.$$
(9)

4.2. Strain-displacement and stress-strain relations

The strain-displacement relation in the Equivalent Single Layer (ESL) model may be described as follows for minor displacements in cylindrical coordinates:

$$\begin{Bmatrix} \mathcal{E}_{\mathbb{r}\mathbb{r}} \\ \mathcal{E}_{\theta\theta} \\ \mathcal{E}_{\mathbb{z}\mathbb{z}} \\ \gamma_{\mathbb{r}\theta} \\ \gamma_{\mathbb{r}\mathbb{z}} \\ \gamma_{\theta\mathbb{z}} \end{Bmatrix} = \begin{bmatrix} \dfrac{\partial}{\partial\mathbb{r}} & 0 & 0 \\ \dfrac{1}{\mathbb{r}} & \dfrac{1}{\mathbb{r}}\left(\dfrac{\partial}{\partial\theta}\right) & 0 \\ 0 & 0 & \dfrac{\partial}{\partial\mathbb{z}} \\ \dfrac{1}{\mathbb{r}}\left(\dfrac{\partial}{\partial\theta}\right) & \dfrac{\partial}{\partial\mathbb{r}} - \dfrac{1}{\mathbb{r}} & 0 \\ \dfrac{\partial}{\partial\mathbb{z}} & 0 & \dfrac{\partial}{\partial\mathbb{r}} \\ 0 & \dfrac{\partial}{\partial\mathbb{z}} & \dfrac{1}{\mathbb{r}}\left(\dfrac{\partial}{\partial\theta}\right) \end{bmatrix} \begin{Bmatrix} \mathbb{u}_\mathbb{r} \\ \mathbb{u}_\theta \\ \mathbb{u}_\mathbb{z} \end{Bmatrix}.$$
(10)

In CUF, the stress and strain vectors are separated into in-plane and normal parts denoted respectively by the subscripts p and n.

$$\boldsymbol{\mathcal{E}}_p^k = \{\mathcal{E}_{\theta\theta} \quad \mathcal{E}_{\mathbb{z}\mathbb{z}} \quad \gamma_{\mathbb{z}\theta}\}^\mathrm{T},$$
$$\boldsymbol{\sigma}_p^k = \{\sigma_{\theta\theta} \quad \sigma_{\mathbb{z}\mathbb{z}} \quad \tau_{\mathbb{z}\theta}\}^\mathrm{T},$$
$$\boldsymbol{\mathcal{E}}_n^k = \{\mathcal{E}_{\mathbb{r}\mathbb{r}} \quad \gamma_{\mathbb{r}\theta} \quad \gamma_{\mathbb{r}\mathbb{z}}\}^\mathrm{T},$$
$$\boldsymbol{\sigma}_n^k = \{\sigma_{\mathbb{r}\mathbb{r}} \quad \tau_{\mathbb{r}\theta} \quad \tau_{\mathbb{r}\mathbb{z}}\}^\mathrm{T}.$$
(11)

Using Equation (10), the strain components $\boldsymbol{\mathcal{E}}_p^k$ and $\boldsymbol{\mathcal{E}}_n^k$ can be related to the displacement field according to the following relations [65].

$$\boldsymbol{\mathcal{E}}_p^k = \left(\frac{1}{\mathbb{r}}\boldsymbol{\mathcal{D}}_{p\theta} + \boldsymbol{\mathcal{D}}_{p\mathbb{z}}\right)\boldsymbol{\mathcal{U}},$$
$$\boldsymbol{\mathcal{E}}_n^k = \left(\boldsymbol{\mathcal{D}}_{n\mathbb{r}} + \frac{1}{\mathbb{r}}\boldsymbol{\mathcal{D}}_{n\Omega\theta} + \boldsymbol{\mathcal{D}}_{n\Omega\mathbb{z}}\right)\boldsymbol{\mathcal{U}},$$
(12)

where $\boldsymbol{\mathcal{D}}_{p\theta}$, $\boldsymbol{\mathcal{D}}_{p\mathbb{z}}$, $\boldsymbol{\mathcal{D}}_{n\mathbb{r}}$, $\boldsymbol{\mathcal{D}}_{n\Omega\theta}$, and $\boldsymbol{\mathcal{D}}_{n\Omega\mathbb{z}}$ are matrix differential operators of the form

$$\boldsymbol{\mathcal{D}}_{p\theta} = \begin{bmatrix} 1 & \dfrac{\partial}{\partial\theta} & 0 \\ 0 & 0 & 0 \\ 0 & 0 & \dfrac{\partial}{\partial\theta} \end{bmatrix}, \boldsymbol{\mathcal{D}}_{p\mathbb{z}} = \begin{bmatrix} 0 & 0 & 0 \\ 0 & 0 & \dfrac{\partial}{\partial\mathbb{z}} \\ 0 & \dfrac{\partial}{\partial\mathbb{z}} & 0 \end{bmatrix},$$

$$\boldsymbol{\mathcal{D}}_{n\mathbb{r}} = \begin{bmatrix} \dfrac{\partial}{\partial\mathbb{r}} & 0 & 0 \\ 0 & \dfrac{\partial}{\partial\mathbb{r}} - \dfrac{1}{\mathbb{r}} & 0 \\ 0 & 0 & \dfrac{\partial}{\partial\mathbb{r}} \end{bmatrix}, \boldsymbol{\mathcal{D}}_{n\Omega\theta} = \begin{bmatrix} 0 & 0 & 0 \\ \dfrac{\partial}{\partial\theta} & 0 & 0 \\ 0 & 0 & 0 \end{bmatrix}, \boldsymbol{\mathcal{D}}_{n\Omega\mathbb{z}} = \begin{bmatrix} 0 & 0 & 0 \\ 0 & 0 & 0 \\ \dfrac{\partial}{\partial\mathbb{z}} & 0 & 0 \end{bmatrix}.$$
(13)

According to Equation (12), the stress-strain relationships at the k$^{\mathrm{th}}$ layer can be represented in the following mixed form:

$$\boldsymbol{\sigma}_p^k = \boldsymbol{\mathcal{C}}_{pp}^k\boldsymbol{\mathcal{E}}_p^k + \boldsymbol{\mathcal{C}}_{pn}^k\boldsymbol{\mathcal{E}}_n^k,$$
$$\boldsymbol{\sigma}_n^k = \boldsymbol{\mathcal{C}}_{np}^k\boldsymbol{\mathcal{E}}_p^k + \boldsymbol{\mathcal{C}}_{nn}^k\boldsymbol{\mathcal{E}}_n^k,$$
(14)

where $\boldsymbol{\mathcal{C}}_{pp}^k$, $\boldsymbol{\mathcal{C}}_{pn}^k$, $\boldsymbol{\mathcal{C}}_{np}^k$, and $\boldsymbol{\mathcal{C}}_{nn}^k$ are matrices of elasticity moduli of the form

$$\boldsymbol{\mathcal{C}}_{pp}^{k} = \begin{bmatrix} \mathcal{C}_{22} & \mathcal{C}_{23} & 0 \\ \mathcal{C}_{32} & \mathcal{C}_{33} & 0 \\ 0 & 0 & \mathcal{C}_{66} \end{bmatrix} = \frac{E_{com}}{(1+\nu_{com})(1-2\nu_{com})} \begin{bmatrix} 1-\nu_{com} & \nu_{com} & 0 \\ \nu_{com} & 1-\nu_{com} & 0 \\ 0 & 0 & \dfrac{1-2\nu_{com}}{2} \end{bmatrix},$$

$$\boldsymbol{\mathcal{C}}_{pn}^{k} = \begin{bmatrix} \mathcal{C}_{21} & 0 & 0 \\ \mathcal{C}_{31} & 0 & 0 \\ 0 & 0 & 0 \end{bmatrix} = \frac{E_{com}}{(1+\nu_{com})(1-2\nu_{com})} \begin{bmatrix} \nu_{com} & 0 & 0 \\ \nu_{com} & 0 & 0 \\ 0 & 0 & 0 \end{bmatrix},$$

$$\boldsymbol{\mathcal{C}}_{np}^{k} = (\boldsymbol{\mathcal{C}}_{pn}^{k})^{\mathrm{T}},$$

$$\boldsymbol{\mathcal{C}}_{nn}^{k} = \begin{bmatrix} \mathcal{C}_{11} & 0 & 0 \\ 0 & \mathcal{C}_{44} & 0 \\ 0 & 0 & \mathcal{C}_{55} \end{bmatrix} = \frac{E_{com}}{(1+\nu_{com})(1-2\nu_{com})} \begin{bmatrix} 1-\nu_{com} & 0 & 0 \\ 0 & \dfrac{1-2\nu_{com}}{2} & 0 \\ 0 & 0 & \dfrac{1-2\nu_{com}}{2} \end{bmatrix}.$$

(15)

Upon substituting Equation (12) into Equation (14), we have

$$\boldsymbol{\sigma}_{p}^{k} = \left[\boldsymbol{\mathcal{C}}_{pp}^{k}\left(\frac{1}{\mathbb{r}}\boldsymbol{\mathcal{D}}_{p\theta} + \boldsymbol{\mathcal{D}}_{pz}\right) + \boldsymbol{\mathcal{C}}_{pn}^{k}\left(\boldsymbol{\mathcal{D}}_{nr} + \frac{1}{\mathbb{r}}\boldsymbol{\mathcal{D}}_{n\Omega\theta} + \boldsymbol{\mathcal{D}}_{n\Omega z}\right)\right]\boldsymbol{\mathcal{U}},$$

$$\boldsymbol{\sigma}_{n}^{k} = \left[\boldsymbol{\mathcal{C}}_{np}^{k}\left(\frac{1}{\mathbb{r}}\boldsymbol{\mathcal{D}}_{p\theta} + \boldsymbol{\mathcal{D}}_{pz}\right) + \boldsymbol{\mathcal{C}}_{nn}^{k}\left(\boldsymbol{\mathcal{D}}_{nr} + \frac{1}{\mathbb{r}}\boldsymbol{\mathcal{D}}_{n\Omega\theta} + \boldsymbol{\mathcal{D}}_{n\Omega z}\right)\right]\boldsymbol{\mathcal{U}}.$$

(16)

Finally, replacing Equation (9) with Equations (12) and (16) yields to:

$$\delta\boldsymbol{\mathcal{E}}_{p}^{k} = \left(\frac{1}{\mathbb{r}}\boldsymbol{\mathcal{D}}_{p\theta} + \boldsymbol{\mathcal{D}}_{pz}\right)\boldsymbol{f}_{\tau}(\mathbb{r})\mathfrak{N}_{i}(\theta,\mathbb{z})\delta\boldsymbol{q}_{\tau i},$$

$$\delta\boldsymbol{\mathcal{E}}_{n}^{k} = \left(\boldsymbol{\mathcal{D}}_{nr} + \frac{1}{\mathbb{r}}\boldsymbol{\mathcal{D}}_{n\Omega\theta} + \boldsymbol{\mathcal{D}}_{n\Omega z}\right)\boldsymbol{f}_{\tau}(\mathbb{r})\mathfrak{N}_{i}(\theta,\mathbb{z})\delta\boldsymbol{q}_{\tau i},$$

$$\boldsymbol{\sigma}_{p}^{k} = \left[\boldsymbol{\mathcal{C}}_{pp}^{k}\left(\frac{1}{\mathbb{r}}\boldsymbol{\mathcal{D}}_{p\theta} + \boldsymbol{\mathcal{D}}_{pz}\right) + \boldsymbol{\mathcal{C}}_{pn}^{k}\left(\boldsymbol{\mathcal{D}}_{nr} + \frac{1}{\mathbb{r}}\boldsymbol{\mathcal{D}}_{n\Omega\theta} + \boldsymbol{\mathcal{D}}_{n\Omega z}\right)\right]\boldsymbol{f}_{s}(\mathbb{r})\mathfrak{N}_{j}(\theta,\mathbb{z})\boldsymbol{q}_{sj},$$

$$\boldsymbol{\sigma}_{n}^{k} = \left[\boldsymbol{\mathcal{C}}_{np}^{k}\left(\frac{1}{\mathbb{r}}\boldsymbol{\mathcal{D}}_{p\theta} + \boldsymbol{\mathcal{D}}_{pz}\right) + \boldsymbol{\mathcal{C}}_{nn}^{k}\left(\boldsymbol{\mathcal{D}}_{nr} + \frac{1}{\mathbb{r}}\boldsymbol{\mathcal{D}}_{n\Omega\theta} + \boldsymbol{\mathcal{D}}_{n\Omega z}\right)\right]\boldsymbol{f}_{s}(\mathbb{r})\mathfrak{N}_{j}(\theta,\mathbb{z})\boldsymbol{q}_{sj}.$$

(17)

5. Radial point interpolation method

As previously stated, the radial point interpolation technique (RPIM) is used to estimate the in-plane displacement field, and the Taylor expansion (Equation (5)) is used to approximate the displacement field across the thickness. The displacement field is interpolated across the dispersed nodes in the support domain using the radial basis shape function in RPIM. As a result, the approximation under consideration, $\mathbb{u}(\theta,\mathbb{z})$, has the shape given by the displacement field function in any direction, $\mathbb{u}(\theta,\mathbb{z})$.

$$\mathbb{u}^{h}(\theta,\mathbb{z}) = \sum_{i=1}^{n_{s}} \mathcal{R}_{i}(\overline{\mathbb{r}}_{I})a_{i} = \boldsymbol{\mathcal{R}}^{\mathrm{T}}(\overline{\mathbb{r}}_{I})\mathbf{a}, \quad (18)$$

where $\mathcal{R}_{i}(\overline{\mathbb{r}}_{I})$ is the radial basis shape functions cantered about point of interest and I is an unknown coefficient, and n_{s} is the number of nodes in the support domain. In cylindrical coordinates, $\overline{\mathbb{r}}_{I}$ is the distance between an arbitrary point and a point of interest.

$$\overline{\mathbb{r}}_{I}^{2} = \mathbb{r}^{2} + \mathbb{r}_{I}^{2} - 2\mathbb{r}\mathbb{r}_{I}\cos(\theta - \theta_{I}) + (\mathbb{z} - \mathbb{z}_{I})^{2}, \quad (19)$$

In this paper, the multiquadrics (MQ) radial basis shape function with the following equation is used [65].

$$\mathcal{R}_{i}(\overline{\mathbb{r}}_{I}) = \left[\overline{\mathbb{r}}_{I}^{2} + c^{2}\right]^{q}, \quad (20)$$

The coefficient vector may be found using the following equation by applying Equation (18) to every node in the support domain.

$$\boldsymbol{q} = \boldsymbol{\mathcal{R}}_{Q}\mathbf{a}, \quad (21)$$

where $\boldsymbol{\mathcal{R}}_{Q}$ is referred to as the moment matrix, whose rows are comprised of nodal values of the radial basis function vector, and vector $\boldsymbol{q}$ is formed of nodal values of the displacement field.

$$\boldsymbol{q}^{\mathrm{T}} = \left\{ \mathbb{u}_{1} \quad \mathbb{u}_{2} \quad \cdots \quad \mathbb{u}_{n_{s}} \right\},$$

$$\boldsymbol{\mathcal{R}}_{Q} = \begin{bmatrix} \mathcal{R}_{1}(\overline{\mathbb{r}}_{1}) & \mathcal{R}_{2}(\overline{\mathbb{r}}_{1}) & \cdots & \mathcal{R}_{n_{s}}(\overline{\mathbb{r}}_{1}) \\ \mathcal{R}_{1}(\overline{\mathbb{r}}_{2}) & \mathcal{R}_{2}(\overline{\mathbb{r}}_{2}) & \cdots & \mathcal{R}_{n_{s}}(\overline{\mathbb{r}}_{2}) \\ \vdots & \vdots & \ddots & \vdots \\ \mathcal{R}_{1}(\overline{\mathbb{r}}_{n_{s}}) & \mathcal{R}_{2}(\overline{\mathbb{r}}_{n_{s}}) & \cdots & \mathcal{R}_{n_{s}}(\overline{\mathbb{r}}_{n_{s}}) \end{bmatrix}, \quad (22)$$

Equation (21), which states that the coefficient vector may be computed as

$$\mathbf{a} = \boldsymbol{\mathcal{R}}_{Q}^{-1}\boldsymbol{q}, \quad (23)$$

The approximation function may be represented in terms of nodal values and radial basis shape functions by substituting the final equation into Equation (18).

$$\mathbb{u}^{h}(\theta,\mathbb{z}) = (\boldsymbol{\mathcal{R}}^{\mathrm{T}}(\overline{\mathbb{r}}_{I})\boldsymbol{\mathcal{R}}_{Q}^{-1})\boldsymbol{q} = \mathfrak{N}^{\mathrm{T}}\boldsymbol{q} = \sum_{i=1}^{\mathfrak{N}_{s}} \mathfrak{N}_{i}\mathbb{u}_{i}. \quad (24)$$

where $\mathfrak{N}_{i}$ is the ith radial basis shape associated with the node i.

6. Governing equation

According to the concept of virtual displacement (PVD), in an equilibrium system, there is no fluctuation in the total potential energy for any virtual displacement field.

$$\delta\mathcal{L}_{\text{int}} + \delta\mathcal{L}_{\text{ine}} + \delta\mathcal{L}_{\text{ext}} = 0. \tag{25}$$

where δ denotes the variational symbol, $\mathcal{L}_{\text{int}}$, $\mathcal{L}_{\text{ine}}$, and $\mathcal{L}_{\text{ext}}$ presents internal virtual work, virtual work of inertial loads, and external virtual work done by external forces, respectively. The variation of internal virtual work for a cylindrical shell may be written as

$$\delta\mathcal{L}_{\text{int}} = \sum_{k=1}^{\mathfrak{N}_l} \int_{V^k} \delta(\boldsymbol{\mathcal{E}}^k)^{\text{T}} \boldsymbol{\sigma}^k dV, \tag{26}$$

where k indicates the layer. Equation (26) can be split into in-plane of the middle surface and through the thickness parts as follow:

$$\delta\mathcal{L}_{\text{int}} = \sum_{k=1}^{\mathfrak{N}_l} \int_{\Omega} \int_{\mathbb{r}_{k-1}}^{\mathbb{r}_k} (\delta(\boldsymbol{\mathcal{E}}_p^k)^{\text{T}} \boldsymbol{\sigma}_p^k + \delta(\boldsymbol{\mathcal{E}}_n^k)^{\text{T}} \boldsymbol{\sigma}_n^k d\mathbb{r}) d\Omega, \tag{27}$$

where $\mathbb{r}$ denotes the through-the-thickness domain and Ω is the layer middle surface of the cylinder. Substitution of Equation (17) into the last equation will lead to a fundamental nucleus form of internal virtual work variation.

$$\delta\mathcal{L}_{\text{int}} = \delta\boldsymbol{q}_{\tau i}^{\text{T}} \boldsymbol{\mathcal{K}}^{ij\tau s} \boldsymbol{q}_{sj}, \tag{28}$$

where $\boldsymbol{\mathcal{K}}^{ij\tau s}$ is the 3×3 fundamental nucleus (FN) of the stiffness matrix according to CUF.

$$\boldsymbol{\mathcal{K}}^{ij\tau s} = \begin{bmatrix} \mathcal{K}_{\mathbb{r}\mathbb{r}} & \mathcal{K}_{\mathbb{r}\theta} & \mathcal{K}_{\mathbb{r}\mathbb{z}} \\ \mathcal{K}_{\theta\mathbb{r}} & \mathcal{K}_{\theta\theta} & \mathcal{K}_{\theta\mathbb{z}} \\ \mathcal{K}_{\mathbb{z}\mathbb{r}} & \mathcal{K}_{\mathbb{z}\theta} & \mathcal{K}_{\mathbb{z}\mathbb{z}} \end{bmatrix}, \tag{29}$$

The FN's components are presented in Equation (30).

$$
\begin{aligned}
\mathcal{K}_{\mathbb{r}\mathbb{r}} &= \int_{\Omega} \mathfrak{N}_i \left(\sum_{k=1}^{\mathfrak{N}_{\mathcal{L}}} \int_{\mathbb{r}_{k-1}}^{\mathbb{r}_k} \mathcal{C}_{21}^k \mathcal{F}_{\tau,\mathbb{r}} \mathcal{F}_s d\mathbb{r} \right) \mathfrak{N}_j d\Omega + \int_{\Omega} \mathfrak{N}_i \left(\sum_{k=1}^{\mathfrak{N}_{\mathcal{L}}} \int_{\mathbb{r}_{k-1}}^{\mathbb{r}_k} \mathcal{C}_{21}^k \mathcal{F}_{\tau} \mathcal{F}_{s,\mathbb{r}} d\mathbb{r} \right) \mathfrak{N}_j d\Omega \\
&+ \int_{\Omega} \mathfrak{N}_i \left(\sum_{k=1}^{\mathfrak{N}_{\mathcal{L}}} \int_{\mathbb{r}_{k-1}}^{\mathbb{r}_k} \mathbb{r}\mathcal{C}_{11}^k \mathcal{F}_{\tau,\mathbb{r}} \mathcal{F}_{s,\mathbb{r}} d\mathbb{r} \right) \mathfrak{N}_j d\Omega + \int_{\Omega} \mathfrak{N}_i \left(\sum_{k=1}^{\mathfrak{N}_{\mathcal{L}}} \int_{\mathbb{r}_{k-1}}^{\mathbb{r}_k} \mathbb{r}\mathcal{C}_{55}^k \mathcal{F}_{\tau,\mathbb{r}} \mathcal{F}_{s,\mathbb{r}} d\mathbb{r} \right) \mathfrak{N}_j d\Omega \\
&+ \int_{\Omega} \mathfrak{N}_i \left(\sum_{k=1}^{\mathfrak{N}_{\mathcal{L}}} \int_{\mathbb{r}_{k-1}}^{\mathbb{r}_k} \mathcal{C}_{22}^k \frac{\mathcal{F}_{\tau} \mathcal{F}_s}{\mathbb{r}} d\mathbb{r} \right) \mathfrak{N}_j d\Omega + \int_{\Omega} \mathfrak{N}_{i,\theta} \left(\sum_{k=1}^{\mathfrak{N}_{\mathcal{L}}} \int_{\mathbb{r}_{k-1}}^{\mathbb{r}_k} \mathcal{C}_{44}^k \frac{\mathcal{F}_{\tau} \mathcal{F}_s}{\mathbb{r}} d\mathbb{r} \right) \mathfrak{N}_{j,\theta} d\Omega,
\end{aligned} \tag{30a}
$$

$$
\begin{aligned}
\mathcal{K}_{\mathbb{r}\theta} &= \int_{\Omega} \mathfrak{N}_i \left(\sum_{k=1}^{\mathfrak{N}_{\mathcal{L}}} \int_{\mathbb{r}_{k-1}}^{\mathbb{r}_k} \mathcal{C}_{21}^k \mathcal{F}_{\tau,\mathbb{r}} \mathcal{F}_s d\mathbb{r} \right) \mathfrak{N}_{j,\theta} d\Omega + \int_{\Omega} \mathfrak{N}_{i,\theta} \left(\sum_{k=1}^{\mathfrak{N}_{\mathcal{L}}} \int_{\mathbb{r}_{k-1}}^{\mathbb{r}_k} \mathcal{C}_{44}^k \mathcal{F}_{\tau} \mathcal{F}_{s,\mathbb{r}} d\mathbb{r} \right) \mathfrak{N}_j d\Omega \\
&+ \int_{\Omega} \mathfrak{N}_i \left(\sum_{k=1}^{\mathfrak{N}_{\mathcal{L}}} \int_{\mathbb{r}_{k-1}}^{\mathbb{r}_k} \mathcal{C}_{22}^k \frac{\mathcal{F}_{\tau} \mathcal{F}_s}{\mathbb{r}} d\mathbb{r} \right) \mathfrak{N}_{j,\theta} d\Omega - \int_{\Omega} \mathfrak{N}_{i,\theta} \left(\sum_{k=1}^{\mathfrak{N}_{\mathcal{L}}} \int_{\mathbb{r}_{k-1}}^{\mathbb{r}_k} \mathcal{C}_{44}^k \frac{\mathcal{F}_{\tau} \mathcal{F}_s}{\mathbb{r}} d\mathbb{r} \right) \mathfrak{N}_j d\Omega,
\end{aligned} \tag{30b}
$$

$$
\mathcal{K}_{\mathbb{r}\mathbb{z}} = \int_{\Omega} \mathfrak{N}_i \left(\sum_{k=1}^{\mathfrak{N}_{\mathcal{L}}} \int_{\mathbb{r}_{k-1}}^{\mathbb{r}_k} \mathcal{C}_{23}^k \mathcal{F}_{\tau} \mathcal{F}_s d\mathbb{r} \right) \mathfrak{N}_{j,\mathbb{z}} d\Omega + \int_{\Omega} \mathfrak{N}_i \left(\sum_{k=1}^{\mathfrak{N}_{\mathcal{L}}} \int_{\mathbb{r}_{k-1}}^{\mathbb{r}_k} \mathbb{r}\mathcal{C}_{31}^k \mathcal{F}_{\tau,\mathbb{r}} \mathcal{F}_s d\mathbb{r} \right) \mathfrak{N}_{j,\mathbb{z}} d\Omega + \int_{\Omega} \mathfrak{N}_i \left(\sum_{k=1}^{\mathfrak{N}_{\mathcal{L}}} \int_{\mathbb{r}_{k-1}}^{\mathbb{r}_k} \mathbb{r}\mathcal{C}_{55}^k \mathcal{F}_{\tau,\mathbb{r}} \mathcal{F}_s d\mathbb{r} \right) \mathfrak{N}_{j,\mathbb{z}} d\Omega,
\tag{30c}
$$

$$\mathcal{K}_{\theta\mathbb{r}} = \int_\Omega \mathfrak{N}_{i,\theta} \left(\sum_{k=1}^{\mathfrak{N}_\mathcal{L}} \int_{\mathbb{r}_{k-1}}^{\mathbb{r}_k} \mathcal{C}_{21}^k \mathfrak{f}_\tau \mathfrak{f}_{s,\mathbb{r}} d\mathbb{r} \right) \mathfrak{N}_j d\Omega + \int_\Omega \mathfrak{N}_i \left(\sum_{k=1}^{\mathfrak{N}_\mathcal{L}} \int_{\mathbb{r}_{k-1}}^{\mathbb{r}_k} \mathcal{C}_{44}^k \mathfrak{f}_{\tau,\mathbb{r}} \mathfrak{f}_s d\mathbb{r} \right) \mathfrak{N}_{j,\theta} d\Omega + \int_\Omega \mathfrak{N}_{i,\theta} \left(\sum_{k=1}^{\mathfrak{N}_\mathcal{L}} \int_{\mathbb{r}_{k-1}}^{\mathbb{r}_k} \mathcal{C}_{22}^k \frac{\mathfrak{f}_\tau \mathfrak{f}_s}{\mathbb{r}} d\mathbb{r} \right) \mathfrak{N}_j d\Omega$$

$$- \int_\Omega \mathfrak{N}_i \left(\sum_{k=1}^{\mathfrak{N}_\mathcal{L}} \int_{\mathbb{r}_{k-1}}^{\mathbb{r}_k} \mathcal{C}_{44}^k \frac{\mathfrak{f}_\tau \mathfrak{f}_s}{\mathbb{r}} d\mathbb{r} \right) \mathfrak{N}_{j,\theta} d\Omega, \tag{30d}$$

$$\mathcal{K}_{\theta\theta} = \int_\Omega \mathfrak{N}_i \left(\sum_{k=1}^{\mathfrak{N}_\mathcal{L}} \int_{\mathbb{r}_{k-1}}^{\mathbb{r}_k} \mathbb{r} \mathcal{C}_{44}^k \mathfrak{f}_{\tau,\mathbb{r}} \mathfrak{f}_{s,\mathbb{r}} d\mathbb{r} \right) \mathfrak{N}_j d\Omega - \int_\Omega \mathfrak{N}_i \left(\sum_{k=1}^{\mathfrak{N}_\mathcal{L}} \int_{\mathbb{r}_{k-1}}^{\mathbb{r}_k} \mathcal{C}_{44}^k \mathfrak{f}_\tau \mathfrak{f}_{s,\mathbb{r}} d\mathbb{r} \right) \mathfrak{N}_j d\Omega - \int_\Omega \mathfrak{N}_i \left(\sum_{k=1}^{\mathfrak{N}_\mathcal{L}} \int_{\mathbb{r}_{k-1}}^{\mathbb{r}_k} \mathcal{C}_{44}^k \mathfrak{f}_{\tau,\mathbb{r}} \mathfrak{f}_s d\mathbb{r} \right) \mathfrak{N}_j d\Omega$$

$$+ \int_\Omega \mathfrak{N}_{i,\mathbb{z}} \left(\sum_{k=1}^{\mathfrak{N}_\mathcal{L}} \int_{\mathbb{r}_{k-1}}^{\mathbb{r}_k} \mathbb{r} \mathcal{C}_{66}^k \mathfrak{f}_\tau \mathfrak{f}_s d\mathbb{r} \right) \mathfrak{N}_{j,\mathbb{z}} d\Omega + \int_\Omega \mathfrak{N}_i \left(\sum_{k=1}^{\mathfrak{N}_\mathcal{L}} \int_{\mathbb{r}_{k-1}}^{\mathbb{r}_k} \mathcal{C}_{44}^k \frac{\mathfrak{f}_\tau \mathfrak{f}_s}{\mathbb{r}} d\mathbb{r} \right) \mathfrak{N}_j d\Omega + \int_\Omega \mathfrak{N}_{i,\theta} \left(\sum_{k=1}^{\mathfrak{N}_\mathcal{L}} \int_{\mathbb{r}_{k-1}}^{\mathbb{r}_k} \mathcal{C}_{22}^k \frac{\mathfrak{f}_\tau \mathfrak{f}_s}{\mathbb{r}} d\mathbb{r} \right) \mathfrak{N}_{j,\theta} d\Omega, \tag{30e}$$

$$\mathcal{K}_{\theta\mathbb{z}} = \int_\Omega \mathfrak{N}_{i,\theta} \left(\sum_{k=1}^{\mathfrak{N}_\mathcal{L}} \int_{\mathbb{r}_{k-1}}^{\mathbb{r}_k} \mathcal{C}_{23}^k \mathfrak{f}_\tau \mathfrak{f}_s d\mathbb{r} \right) \mathfrak{N}_{j,\mathbb{z}} d\Omega + \int_\Omega \mathfrak{N}_{i,\mathbb{z}} \left(\sum_{k=1}^{\mathfrak{N}_\mathcal{L}} \int_{\mathbb{r}_{k-1}}^{\mathbb{r}_k} \mathcal{C}_{66}^k \mathfrak{f}_\tau \mathfrak{f}_s d\mathbb{r} \right) \mathfrak{N}_{j,\theta} d\Omega, \tag{30f}$$

$$\mathcal{K}_{\mathbb{z}\mathbb{r}} = \int_\Omega \mathfrak{N}_{i,\mathbb{z}} \left(\sum_{k=1}^{\mathfrak{N}_\mathcal{L}} \int_{\mathbb{r}_{k-1}}^{\mathbb{r}_k} \mathcal{C}_{23}^k \mathfrak{f}_\tau \mathfrak{f}_s d\mathbb{r} \right) \mathfrak{N}_j d\Omega + \int_\Omega \mathfrak{N}_{i,\mathbb{z}} \left(\sum_{k=1}^{\mathfrak{N}_\mathcal{L}} \int_{\mathbb{r}_{k-1}}^{\mathbb{r}_k} \mathbb{r} \mathcal{C}_{31}^k \mathfrak{f}_\tau \mathfrak{f}_{s,\mathbb{r}} d\mathbb{r} \right) \mathfrak{N}_j d\Omega + \int_\Omega \mathfrak{N}_{i,\mathbb{z}} \left(\sum_{k=1}^{\mathfrak{N}_\mathcal{L}} \int_{\mathbb{r}_{k-1}}^{\mathbb{r}_k} \mathbb{r} \mathcal{C}_{55}^k \mathfrak{f}_\tau \mathfrak{f}_{s,\mathbb{r}} d\mathbb{r} \right) \mathfrak{N}_j d\Omega, \tag{30g}$$

$$\mathcal{K}_{\mathbb{z}\theta} = \int_\Omega \mathfrak{N}_{i,\mathbb{z}} \left(\sum_{k=1}^{\mathfrak{N}_\mathcal{L}} \int_{\mathbb{r}_{k-1}}^{\mathbb{r}_k} \mathcal{C}_{23}^k \mathfrak{f}_\tau \mathfrak{f}_s d\mathbb{r} \right) \mathfrak{N}_{j,\theta} d\Omega + \int_\Omega \mathfrak{N}_{i,\theta} \left(\sum_{k=1}^{\mathfrak{N}_\mathcal{L}} \int_{\mathbb{r}_{k-1}}^{\mathbb{r}_k} \mathcal{C}_{66}^k \mathfrak{f}_\tau \mathfrak{f}_s d\mathbb{r} \right) \mathfrak{N}_{j,\mathbb{z}} d\Omega, \tag{30h}$$

$$\mathcal{K}_{\mathbb{z}\mathbb{z}} = \int_\Omega \mathfrak{N}_{i,\mathbb{z}} \left(\sum_{k=1}^{\mathfrak{N}_\mathcal{L}} \int_{\mathbb{r}_{k-1}}^{\mathbb{r}_k} \mathbb{r} \mathcal{C}_{33}^k \mathfrak{f}_\tau \mathfrak{f}_s d\mathbb{r} \right) \mathfrak{N}_{j,\mathbb{z}} d\Omega + \int_\Omega \mathfrak{N}_{i,\mathbb{z}} \left(\sum_{k=1}^{\mathfrak{N}_\mathcal{L}} \int_{\mathbb{r}_{k-1}}^{\mathbb{r}_k} \mathbb{r} \mathcal{C}_{55}^k \mathfrak{f}_\tau \mathfrak{f}_s d\mathbb{r} \right) \mathfrak{N}_{j,\mathbb{z}} d\Omega + \int_\Omega \mathfrak{N}_{i,\theta} \left(\sum_{k=1}^{\mathfrak{N}_\mathcal{L}} \int_{\mathbb{r}_{k-1}}^{\mathbb{r}_k} \mathcal{C}_{66}^k \frac{\mathfrak{f}_\tau \mathfrak{f}_s}{\mathbb{r}} d\mathbb{r} \right) \mathfrak{N}_{j,\theta} d\Omega, \tag{30i}$$

The generalized form of the work produced by the foundation and friction force is:

$$\delta \mathcal{L}_{ext} = \int_\Omega \delta \mathbb{u}_\mathbb{r}(R_o, \theta, \mathbb{z}) \wp(R_o, \theta, \mathbb{z}) d\Omega + \int_\Omega \delta \mathbb{u}_\theta(R_o, \theta, \mathbb{z}) \wp_\mathbb{r}(R_o, \theta, \mathbb{z}) d\Omega + \int_\Omega \delta \mathbb{u}_\mathbb{z}(R_o, \theta, \mathbb{z}) \mathfrak{f}_\mathcal{T}(R_o, \theta, \mathbb{z}) d\Omega, \tag{31}$$

The variation of work done due to foundation can be achieved from the following equations:

$$\wp(R_o, \theta, \mathbb{z}) = \mathrm{K}_{wo}(R_o, \theta, \mathbb{z}) \mathbb{u}_\mathbb{r} - \frac{\partial}{\partial \mathbb{z}} \left(K_{po}(R_o, \theta, \mathbb{z}) \frac{\partial \mathbb{u}_\mathbb{r}}{\partial \mathbb{z}} \right) - \frac{1}{R^2} \frac{\partial}{\partial \theta} \left(K_{po}(R_o, \theta, \mathbb{z}) \frac{\partial \mathbb{u}_\mathbb{r}}{\partial \theta} \right), \tag{32}$$

Where $K_{wo}(R_o, \theta, \mathbb{z})$, and $K_{po}(R_o, \theta, \mathbb{z})$ represent the coordinate-dependent Winkler–Pasternak coefficients. For linear elastic foundation:

$$K_{wo}(x, y, \mathbb{z}) = K_w \times \left(1 + \mathfrak{L}_1 \left(\frac{\mathbb{z}}{a}\right) + \mathfrak{L}_2 \left(\frac{\mathbb{z}}{a}\right)^2 \right) \times \left(1 + \mathfrak{L}_1 \left(\frac{\theta}{2\pi}\right) + \mathfrak{L}_2 \left(\frac{\theta}{2\pi}\right)^2 \right), \tag{33a}$$

$$K_{po}(x, y, \mathbb{z}) = K_p \times \left(1 + \mathfrak{L}_1 \left(\frac{\mathbb{z}}{a}\right) + \mathfrak{L}_2 \left(\frac{\mathbb{z}}{a}\right)^2 \right) \times \left(1 + \mathfrak{L}_1 \left(\frac{\theta}{2\pi}\right) + \mathfrak{L}_2 \left(\frac{\theta}{2\pi}\right)^2 \right). \tag{33b}$$

K_w, and K_p represent the elastic coefficients of the Winkler–Pasternak foundation. Also, $\mathfrak{L}_1$, and $\mathfrak{L}_2$ shows constant values for linear and torsional elastic foundations.

For sinusoidal elastic foundation:

$$K_{wo}(x,y,\mathbb{z}) = K_w \times \left(1 + \mathcal{L}_1\left(\sin\left(\frac{\pi\mathbb{z}}{a}\right)\right) + \mathcal{L}_2\left(\sin\left(\frac{\pi\mathbb{z}}{a}\right)\right)^2\right)$$
$$\times \left(1 + \mathcal{L}_1\left(\sin\left(\frac{\theta}{2}\right)\right) + \mathcal{L}_2\left(\sin\left(\frac{\theta}{2}\right)\right)^2\right),$$
(34a)

$$K_{po}(x,y,\mathbb{z}) = K_p \times \left(1 + \mathcal{L}_1\left(\sin\left(\frac{\pi\mathbb{z}}{a}\right)\right) + \mathcal{L}_2\left(\sin\left(\frac{\pi\mathbb{z}}{a}\right)\right)^2\right)$$
$$\times \left(1 + \mathcal{L}_1\left(\sin\left(\frac{\theta}{2}\right)\right) + \mathcal{L}_2\left(\sin\left(\frac{\theta}{2}\right)\right)^2\right).$$
(34b)

For cosinusoidal elastic foundation:

$$K_{wo}(x,y,\mathbb{z}) = K_w \times \left(1 + \mathcal{L}_1\left(\cos\left(\frac{\pi\mathbb{z}}{a}\right)\right) + \mathcal{L}_2\left(\cos\left(\frac{\pi\mathbb{z}}{a}\right)\right)^2\right)$$
$$\times \left(1 + \mathcal{L}_1\left(\cos\left(\frac{\theta}{2}\right)\right) + \mathcal{L}_2\left(\cos\left(\frac{\theta}{2}\right)\right)^2\right),$$
(35a)

$$K_{po}(x,y,\mathbb{z}) = K_p \times \left(1 + \mathcal{L}_1\left(\cos\left(\frac{\pi\mathbb{z}}{a}\right)\right) + \mathcal{L}_2\left(\cos\left(\frac{\pi\mathbb{z}}{a}\right)\right)^2\right)$$
$$\times \left(1 + \mathcal{L}_1\left(\cos\left(\frac{\theta}{2}\right)\right) + \mathcal{L}_2\left(\cos\left(\frac{\theta}{2}\right)\right)^2\right),$$
(35b)

The torsional elastic foundation can be written as below:

$$\wp_{\mathbb{r}}\left(\mathbb{r}_{top}, \theta, \mathbb{z}\right) = K_{\mathbb{r}10}(R_o, \theta, \mathbb{z})\phi - \frac{\partial}{\partial z}\left(K_{\mathbb{r}20}(R_o, \theta, \mathbb{z})\frac{\partial\phi}{\partial z}\right),$$
(36)

$K_{\mathbb{r}10}(R_o, \theta, \mathbb{z})$, and $K_{\mathbb{r}20}(R_o, \theta, \mathbb{z})$ represent the coordinate-dependent torsional stiffness of the foundation.

Substituting $\phi = \frac{\partial\mathbb{u}_\theta}{\partial\mathbb{z}}$ into Equation (36) leads to:

$$\wp_{\mathbb{r}}(R_o, \theta, \mathbb{z}) = K_{\mathbb{r}10}(R_o, \theta, \mathbb{z})\frac{\partial\mathbb{u}_\theta}{\partial\mathbb{z}} - \frac{\partial}{\partial\mathbb{z}}\left(K_{\mathbb{r}20}(R_o, \theta, \mathbb{z})\frac{\partial^2\mathbb{u}_\theta}{\partial\mathbb{z}^2}\right),$$
(37)

For linear torsional elastic foundation:

$$K_{\mathbb{r}10}(R_o, \theta, \mathbb{z}) = K_{\mathbb{r}1} \times \left(1 + \mathcal{L}_1\left(\frac{\mathbb{z}}{a}\right) + \mathcal{L}_2\left(\frac{\mathbb{z}}{a}\right)^2\right)$$
$$\times \left(1 + \mathcal{L}_1\left(\frac{\theta}{2\pi}\right) + \mathcal{L}_2\left(\frac{\theta}{2\pi}\right)^2\right),$$
(38a)

$$K_{\mathbb{r}20}(R_o, \theta, \mathbb{z}) = K_{\mathbb{r}2} \times \left(1 + \mathcal{L}_1\left(\frac{\mathbb{z}}{a}\right) + \mathcal{L}_2\left(\frac{\mathbb{z}}{a}\right)^2\right)$$
$$\times \left(1 + \mathcal{L}_1\left(\frac{\theta}{2\pi}\right) + \mathcal{L}_2\left(\frac{\theta}{2\pi}\right)^2\right).$$
(38b)

$K_{\mathbb{r}1}$, and $K_{\mathbb{r}2}$ represent the torsional coefficients of the foundation.

For sinusoidal torsional elastic foundation:

$$K_{\mathbb{r}10}(R_o, \theta, \mathbb{z}) = K_{\mathbb{r}1} \times \left(1 + \mathcal{L}_1\left(\sin\left(\frac{\pi\mathbb{z}}{a}\right)\right) + \mathcal{L}_2\left(\sin\left(\frac{\pi\mathbb{z}}{a}\right)\right)^2\right)$$
$$\times \left(1 + \mathcal{L}_1\left(\sin\left(\frac{\theta}{2}\right)\right) + \mathcal{L}_2\left(\sin\left(\frac{\theta}{2}\right)\right)^2\right),$$
(39a)

$$K_{\mathbb{r}20}(R_o, \theta, \mathbb{z}) = K_{\mathbb{r}2} \times \left(1 + \mathcal{L}_1\left(\sin\left(\frac{\pi\mathbb{z}}{a}\right)\right) + \mathcal{L}_2\left(\sin\left(\frac{\pi\mathbb{z}}{a}\right)\right)^2\right)$$
$$\times \left(1 + \mathcal{L}_1\left(\sin\left(\frac{\theta}{2}\right)\right) + \mathcal{L}_2\left(\sin\left(\frac{\theta}{2}\right)\right)^2\right).$$
(39b)

For cosinusoidal torsional elastic foundation:

$$K_{\mathbb{r}10}(R_o, \theta, \mathbb{z}) = K_{\mathbb{r}1} \times \left(1 + \mathcal{L}_1\left(\cos\left(\frac{\pi\mathbb{z}}{a}\right)\right) + \mathcal{L}_2\left(\cos\left(\frac{\pi\mathbb{z}}{a}\right)\right)^2\right)$$
$$\times \left(1 + \mathcal{L}_1\left(\cos\left(\frac{\theta}{2}\right)\right) + \mathcal{L}_2\left(\cos\left(\frac{\theta}{2}\right)\right)^2\right),$$
(40a)

$$K_{\mathbb{r}20}(R_o, \theta, \mathbb{z}) = K_{\mathbb{r}2} \times \left(1 + \mathcal{L}_1\left(\cos\left(\frac{\pi\mathbb{z}}{a}\right)\right) + \mathcal{L}_2\left(\cos\left(\frac{\pi\mathbb{z}}{a}\right)\right)^2\right)$$
$$\times \left(1 + \mathcal{L}_1\left(\cos\left(\frac{\theta}{2}\right)\right) + \mathcal{L}_2\left(\cos\left(\frac{\theta}{2}\right)\right)^2\right),$$
(40b)

The frictional force is regarded as (A. B. 66]

$$\mathbb{f}_{\mathcal{T}}(R_o, \theta, \mathbb{z}) = \mu_{\mathcal{T}}\left(K_{wo}(R_o, \theta, \mathbb{z})\mathbb{u}_{\mathbb{z}} - \frac{\partial}{\partial\mathbb{z}}\left(K_{po}(R_o, \theta, \mathbb{z})\frac{\partial\mathbb{u}_{\mathbb{z}}}{\partial\mathbb{z}}\right)\right.$$
$$\left. - \frac{1}{R^2}\frac{\partial}{\partial\theta}\left(K_{po}(R_o, \theta, \mathbb{z})\frac{\partial\mathbb{u}_{\mathbb{z}}}{\partial\theta}\right)\right).$$
(41)

$\mu_{\mathcal{T}}$ denotes the foundation friction coefficient.

where R_o is associated with the upper coordinate of a cross-section in r and R_o is lift given in Equation (5). In the Carrera Unified Formulation framework, external work can be written as:

$$\delta\mathcal{L}_{ext} = \delta\boldsymbol{q}_{\tau i}^T \boldsymbol{K}_a^{ij\tau s} \boldsymbol{q}_{sj},$$
(42)

where $K_a^{ij\tau s}$

$$\mathcal{K}_a^{ij\tau s} = \begin{bmatrix} \mathcal{K}_{\mathbb{r}\mathbb{r}a} & 0 & 0 \\ 0 & \mathcal{K}_{\theta\theta a} & 0 \\ 0 & 0 & \mathcal{K}_{\mathbb{z}\mathbb{z}a} \end{bmatrix}, \quad (43)$$

$\mathcal{K}_a^{ij\tau s}$ (stiffness) are contributions due to the foundation and friction force.

The virtual variation of the work of inertial loads can be obtained as follows.

$$\delta\mathcal{L}_{\text{ine}} = \delta\boldsymbol{q}_{\tau i}^{\text{T}}\boldsymbol{M}^{ij\tau s}\ddot{\boldsymbol{q}}_{sj}, \quad (44)$$

where $\ddot{\boldsymbol{q}}_{sj}$ is the acceleration of the nucleus at all nodes located in the support domain and $\boldsymbol{M}^{ij\tau s}$ is the mass matrix which is a diagonal matrix given by

$$\boldsymbol{M}^{ij\tau s} = \begin{bmatrix} \mathcal{M}_{\mathbb{r}\mathbb{r}} & 0 & 0 \\ 0 & \mathcal{M}_{\theta\theta} & 0 \\ 0 & 0 & \mathcal{M}_{\mathbb{z}\mathbb{z}} \end{bmatrix}, \quad (45)$$

Where

$$\mathcal{M}_{\mathbb{r}\mathbb{r}} = \mathcal{M}_{\theta\theta} = \mathcal{M}_{\mathbb{z}\mathbb{z}} = \int_{\Omega} \mathfrak{N}_i \left(\sum_{k=1}^{\mathfrak{N}_a} \int_{\mathbb{r}_{k-1}}^{\mathbb{r}_k} \rho_{com} F_\tau F_s d\mathbb{r} \right) \mathfrak{N}_j d\Omega, \quad (46)$$

in which ρ_{com} is the mass density of layer k.

Thus, the equation of motion can be formally put in the following compact form:

$$\left(\mathcal{K}^{ij\tau s} + \mathcal{K}_a^{ij\tau s}\right)\boldsymbol{q}_{sj} + \boldsymbol{M}^{ij\tau s}\ddot{\boldsymbol{q}}_{sj} = 0. \quad (47)$$

As far as t

$$\boldsymbol{q}_{sj} = \boldsymbol{\mathcal{Q}}_{sj}e^{i\omega t}, \quad (48)$$

where $\boldsymbol{\mathcal{Q}}_{sj}$ is the amplitude of displacement unknowns; ω is the angular frequency; and i^2 is equal to -1. By substituting Equation (48) into Equation (47), a linear system of the algebraic equations of motion is given by:

$$\left[\left(\mathcal{K}^{ij\tau s} + \mathcal{K}_a^{ij\tau s}\right) - \omega^2 \boldsymbol{M}^{ij\tau s}\right]\boldsymbol{\mathcal{Q}}_{sj} = 0. \quad (49)$$

By solving Equation (49), the eigenvalue and eigenvector of the system can be achieved. Moreover, the dimensionless parameters have the following definitions:

$$K_w^* = \frac{K_w \mathcal{R}^5}{E_m I}, K_p^* = \frac{K_p \mathcal{R}^3}{E_m I}, \overline{\omega} = \omega\sqrt{\frac{\rho_m}{E_m}}, R = \frac{R_i + R_o}{2}. \quad (50)$$

7. Result

7.1. Validation with nondestructive testing

Table 1 reflects a comparison between the numerically computed and experimentally observed first ten natural frequencies of a cylindrical isotropic homogeneous panel subjected to clamped boundary conditions along all edges. The numerical frequencies, referred to as the "Present" values, are calculated using specific geometric and material parameters, including a panel length of 0.0762 m, a width of 0.1016 m, and a thickness of 0.03302 cm. The panel exhibits a curvature radius of

Table 1. First ten frequencies $\Omega = \omega/2\pi$ of CCCC isotropic homogeneous panels with $a = 0.0762$ [m], $S = 0.1016$ [m], $h = 0.03302$ [cm], $R = 0.762$ [m], $E = 68.947$ [GPa], $\rho = 2657.27$ [kg/m³] and $\nu = 0.33$.

Ω	Present	Experimental [67]
Ω_1	870	814
Ω_2	958	940
Ω_3	1289	1260
Ω_4	1365	1306
Ω_5	1441	1452
Ω_6	1755	1770
Ω_7	1780	1802
Ω_8	2059	2100
Ω_9	2221	2225
Ω_{10}	2290	2280

0.762 m, consistent with its cylindrical geometry. Material properties such as Young's modulus of 68.947 GPa, a density of 2657.27 kg/m³, and a Poisson's ratio of 0.33 further define the mechanical behavior of the structure. The calculated frequencies show a strong correlation with the experimental data, suggesting that the numerical model captures the essential dynamics of the system. The numerical results for the first natural frequency yield a value of 870 Hz, slightly higher than the experimentally obtained 814 Hz. A similar trend is observed across subsequent modes, with minor deviations becoming more pronounced at higher frequencies. For example, the numerical value for the fifth mode is 1441 Hz, while the experimental counterpart is 1452 Hz, indicating a slight underestimation. As the frequency modes increase, these deviations remain within acceptable ranges, as demonstrated by the tenth mode, where the numerical value is 2290 Hz compared to the experimental 2280 Hz. The small discrepancies between the two sets of data may be attributed to several factors, including model simplifications, assumptions in boundary conditions, or potential inaccuracies in experimental measurements. Nonetheless, the close agreement between the computed and measured frequencies validates the robustness of the numerical approach, demonstrating its efficacy for vibration analysis in complex structures such as isotropic homogeneous panels under clamped conditions. The results further underscore the importance of numerical methods in predicting dynamic behavior in engineering structures, providing engineers with valuable tools for design optimization and structural integrity assessment.

7.2. Introduction to deep neural networks for predicting vibration analysis of nanocomposite-enhanced bridge structures validated by nondestructive testing

Nanocomposite-enhanced bridge structures represent a new frontier in civil engineering, particularly in the pursuit of more resilient, durable, and lightweight materials for construction. These advanced materials often incorporate nanoparticles, such as carbon nanotubes or graphene, which improve the mechanical properties of traditional construction materials, such as concrete and steel, by enhancing their stiffness, strength, and durability. As such, vibration analysis of these structures is critical for assessing their stability, safety, and performance, especially under dynamic loads such as

traffic or environmental forces. However, the complexity of nanocomposite materials introduces new challenges in accurately predicting the vibration response of these structures. This is where the application of deep neural networks (DNNs) becomes highly relevant. DNNs, a subset of machine learning techniques, are particularly adept at handling large, complex datasets and identifying intricate patterns within them. In the context of vibration analysis for nanocomposite-enhanced bridge structures, DNNs can be used to model the complex, nonlinear relationships between material properties, structural configurations, and vibrational behavior. By training on datasets that encompass various bridge designs, material compositions, and environmental conditions, DNNs can learn to predict how a bridge will respond to different types of vibrations with high accuracy. The integration of nondestructive testing (NDT) methods with DNN predictions further enhances the reliability and practicality of vibration analysis. NDT techniques, such as ultrasonic testing, acoustic emission, and thermography, allow engineers to evaluate the structural health of bridges without causing any damage or disruption to the infrastructure. These techniques can provide real-time data about the condition of a bridge, which can then be fed into a DNN model. This combination allows for a more accurate prediction of potential failure points, stress concentrations, or other weaknesses that may not be detectable through traditional analysis methods alone. Moreover, the use of DNNs in this context offers several key advantages. First, DNN models can improve over time as more data is collected from NDT and field observations, making the predictive models more robust and reliable. Second, DNNs are capable of generalizing across different bridge structures and nanocomposite materials, providing a flexible tool that can be applied to a wide range of scenarios. Finally, DNNs can be used in real-time applications, enabling continuous monitoring of bridge health and providing early warnings of potential issues before they become critical. In conclusion, the use of deep neural networks for predicting the vibration analysis of nanocomposite-enhanced bridge structures, when combined with nondestructive testing methods, represents a powerful approach for ensuring the long-term safety and stability of modern infrastructure. By leveraging the strengths of both advanced materials and cutting-edge machine learning techniques, engineers can develop more accurate, efficient, and reliable systems for monitoring and maintaining the integrity of critical structures like bridges, ultimately contributing to safer and more resilient civil infrastructure. A Python code of the presented algorithm is shown in Figure 2.

```python
pip install tensorflow scikit-learn
import numpy as np
import tensorflow as tf
from tensorflow.keras.models import Sequential
from tensorflow.keras.layers import Dense
from sklearn.model_selection import train_test_split
from sklearn.preprocessing import StandardScaler
# Simulated data generation
# Assume we have features like material properties, structural configs, and NDT results
np.random.seed(42)
n_samples = 1000
n_features = 10  # number of input features (e.g., material properties, NDT results)
# Generate random data for input features (X) and target vibration response (y)
X = np.random.rand(n_samples, n_features)  # feature matrix
y = np.random.rand(n_samples, 1)  # target vibration response
# Preprocess the data (standardization)
scaler = StandardScaler()
X_scaled = scaler.fit_transform(X)
# Split data into training and testing sets
X_train, X_test, y_train, y_test = train_test_split(X_scaled, y, test_size=0.2, random_state=42)
# Build the Deep Neural Network (DNN) model
model = Sequential([
    Dense(64, input_dim=n_features, activation='relu'),  # input layer
    Dense(128, activation='relu'),  # hidden layer 1
    Dense(128, activation='relu'),  # hidden layer 2
    Dense(64, activation='relu'),  # hidden layer 3
    Dense(1)  # output layer (predicting vibration response)])
# Compile the model
model.compile(optimizer='adam', loss='mean_squared_error')
# Train the model
history = model.fit(X_train, y_train, epochs=100, batch_size=32, validation_data=(X_test, y_test))
# Evaluate the model on test data
loss = model.evaluate(X_test, y_test)
print(f"Test Loss (Mean Squared Error): {loss}")
# Make predictions
y_pred = model.predict(X_test)
# Output first few predicted values and compare with actual values
print(f"Predicted Vibration Response: {y_pred[:5].flatten()}")
print(f"Actual Vibration Response: {y_test[:5].flatten()}")
```

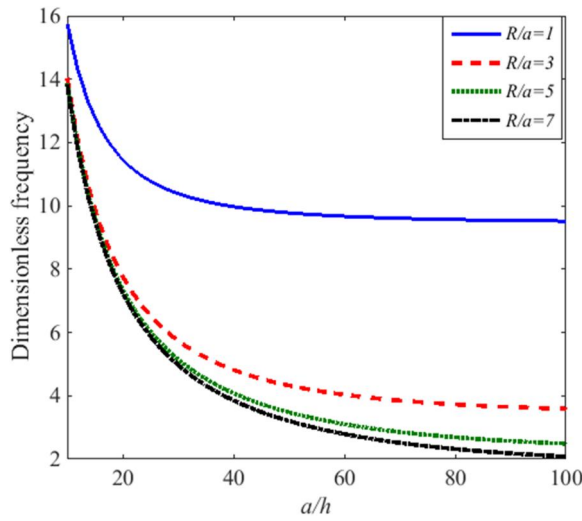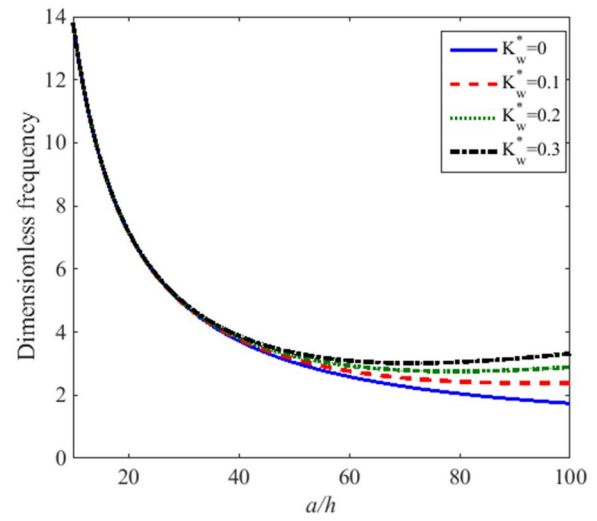**Figure 2.** A Python code of the presented algorithm.

Figure 3. Dimensionless frequency of a panel structure reinforced by Al_2O_3 nanocomposite for various a/h and R/a ratios.

Figure 4. Dimensionless frequency of a panel structure reinforced by Al_2O_3 nanocomposite for various a/h and K_W^* ratios.

7.3. Parametric results

Figure 3 presents the variation of the dimensionless frequency as a function of the length-to-thickness ratio (a/h) for a curved Al_2O_3 nanocomposite-reinforced bridge concrete structure surrounded by an elastic substrate. The graph plots four curves corresponding to different dimensionless radius curvature factors (R/a), specifically 1, 3, 5, and 7. The horizontal axis represents the length-to-thickness ratio, while the vertical axis indicates the dimensionless frequency. As the length-to-thickness ratio increases, a decreasing trend in dimensionless frequency is observed for all curvature factors. At lower values of a/h, the structure exhibits higher frequencies, particularly for $R/a = 1$, where the frequency remains significantly higher across the range of a/h values. As R/a increases, the dimensionless frequency decreases more rapidly with increasing a/h, highlighting a sensitivity of frequency to changes in the radius curvature factor (RFC). This implies that higher curvature values (lower R/a) enhance the stiffness of the structure, leading to elevated frequencies. Additionally, the elastic foundation parameters, represented by the dimensionless Winkler coefficient (K_W^*) and Pasternak coefficient (K_P^*), likely influence this behavior by contributing to the overall stiffness. The interplay between the radius curvature factor and the elastic substrate suggests that structures with lower R/a are more resistant to deformation, which directly affects the vibration characteristics of the nanocomposite structure. These results provide critical insights into the design and optimization of curved surfaces in bridge applications, where frequency response plays a significant role in structural stability and performance.

Figure 4 illustrates the relationship between the dimensionless frequency and the length-to-thickness ratio for a curved Al_2O_3 nanocomposite reinforced bridge concrete structure, with varying dimensionless Winkler coefficients. The x-axis represents the length-to-thickness ratio (a/h), while the y-axis displays the dimensionless frequency. The plot includes four curves, each representing a different value of the Winkler coefficient, specifically 0, 0.1, 0.2, and 0.3. As a/h increases, the dimensionless frequency decreases for all values of K_W^*. In
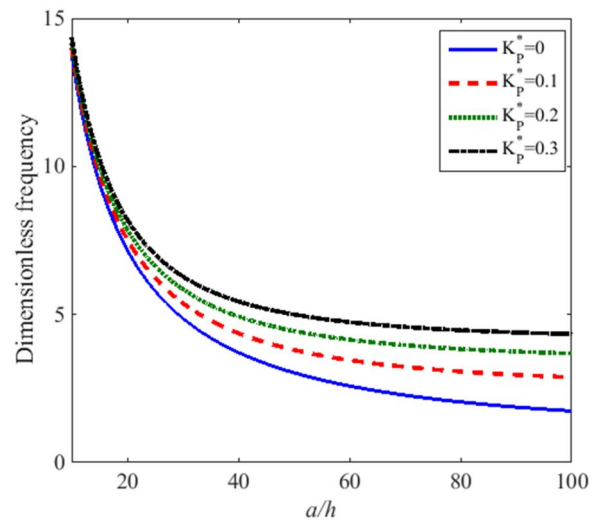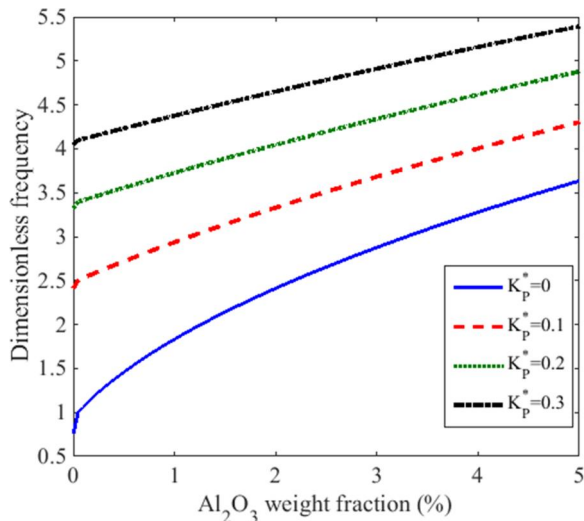

Figure 5. Dimensionless frequency of a panel structure reinforced by Al_2O_3 nanocomposite for various a/h and K_P^* ratios.

the case of $K_W^* = 0$, where the elastic substrate has no stiffness contribution, the frequency decreases more sharply compared to other cases. As the Winkler coefficient increases, representing a stiffer elastic foundation, the dimensionless frequency for the structure also increases. The curve corresponding to $K_W^* = 0.3$ shows the highest frequency values, suggesting that the elastic substrate significantly enhances the overall stiffness of the structure, thereby raising its natural frequencies. The sensitivity of the dimensionless frequency to the Winkler coefficient is more pronounced at lower values of a/h. As the length-to-thickness ratio increases, the curves for different values of K_W^* begin to converge, indicating a diminished influence of the elastic foundation stiffness for thinner structures (larger a/h). The results suggest that the Winkler foundation model plays an important role in the vibration characteristics of the nanocomposite structure, particularly in the design of bridges where the support conditions and foundation stiffness are critical factors affecting dynamic performance.

Figure 5 presents the relationship between dimensionless frequency and the length-to-thickness ratio for a curved Al_2O_3 nanocomposite-reinforced bridge concrete structure with varying dimensionless Pasternak coefficients. The x-axis represents the length-to-thickness ratio, while the y-axis shows the dimensionless frequency. Four curves are plotted, corresponding to different values of the Pasternak coefficient: $K_P^* =$ 0, 0.1, 0.2, and 0.3. As a/h increases, the dimensionless frequency decreases for all values of K_P^*, similar to previous trends with increasing structural thickness. The lowest curve represents $K_P^* = 0$, which indicates no contribution from the shear layer in the elastic substrate. As the Pasternak coefficient increases, there is a noticeable rise in the dimensionless frequency, with $K_P^* = 0.3$ showing the highest frequencies. This trend suggests that the shear interaction modeled by the Pasternak foundation adds stiffness to the structure, increasing its natural frequencies. The sensitivity of the dimensionless frequency to the Pasternak coefficient is especially prominent for lower values of a/h, where thicker structures are more influenced by the substrate's shear effects. As the a/h ratio increases, indicating a thinner structure, the curves begin to converge, signifying a reduced impact of the Pasternak coefficient on the frequency. This observation implies that the shear layer contribution from the foundation becomes less significant for slender structures. These results are important for optimizing bridge designs with composite materials, where the foundation's shear stiffness must be considered for dynamic response and stability.

Figure 6 illustrates the dimensionless frequency variation of an Al_2O_3 nanocomposite-reinforced concrete bridge structure surrounded by an elastic substrate, where the elastic foundation is characterized by both Winkler and Pasternak coefficients. The horizontal axis represents the Al_2O_3 weight fraction (0–5%), while the vertical axis shows the dimensionless frequency. Multiple curves are plotted to correspond to different values of the dimensionless Pasternak coefficient, ranging from 0 to 0.3, indicating its effect on the frequency response of the structure. As the Al_2O_3 weight fraction

increases, the dimensionless frequency increases for all values of K_P^*. Specifically, the lowest curve (blue) corresponds to $K_P^* = 0$, while the highest curve (black) corresponds to $K_P^* =$ 0.3, demonstrating that increasing K_P^* enhances the frequency response. This trend implies a significant sensitivity of the structure's dynamic behavior to the Pasternak coefficient. The presence of the Al_2O_3 reinforcement improves the stiffness of the nanocomposite, leading to higher frequencies. In terms of the radius of curvature factor, R/a, and the length-to-thickness ratio, a/h, the frequency response is expected to further vary depending on these structural parameters, which are not explicitly plotted here but contribute to the overall sensitivity. RFC, or the sensitivity of frequency to radius curvature factor, can be influenced by the interaction between these parameters and the elastic foundation characterized by the Winkler and Pasternak coefficients, further impacting the mechanical behavior of the curved composite surface.

Figure 7 illustrates the relationship between dimensionless frequency and Al_2O_3 weight fraction (%) for various values of the dimensionless radius of curvature factor, in an Al_2O_3 nanocomposite reinforced concrete bridge structure. The structure is surrounded by an elastic substrate. The horizontal axis shows the Al_2O_3 weight fraction (0–5%), while the vertical axis represents the dimensionless frequency. Different curves correspond to varying values of R/a, the ratio of the radius of curvature to the characteristic length. The blue curve represents $R/a = 1$, the red dashed curve corresponds to $R/a = 3$, the green dotted curve to $R/a = 5$, and the black dashed curve to $R/a = 7$. The figure indicates that as the Al_2O_3 weight fraction increases, the dimensionless frequency increases for all values of R_x/a. However, the sensitivity of the frequency to the Al_2O_3 reinforcement diminishes as R_x/a increases. For $R/a = 1$, the frequency shows a steep increase, implying that structures with a lower radius of curvature (more curved) exhibit a stronger frequency response to the increase in Al_2O_3 weight fraction. In contrast, for higher values of R/a (i.e. $R/a = 7$, the frequency response is more gradual, indicating that flatter structures are less sensitive to changes in
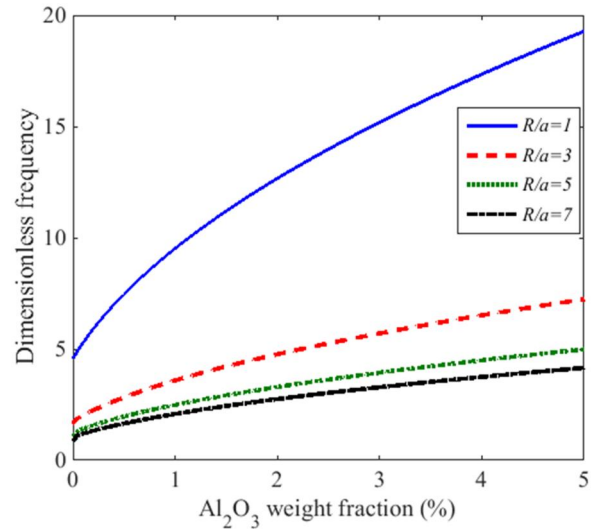

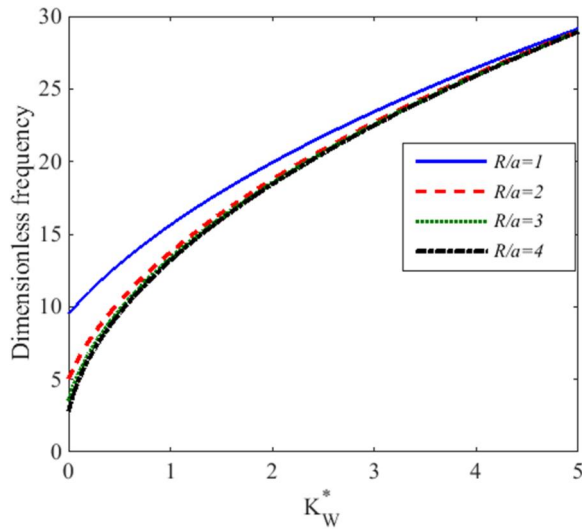**Figure 6.** Dimensionless frequency of a panel structure reinforced by Al_2O_3 nanocomposite for various Al_2O_3 weight fractions and K_P^* ratios.

Figure 7. Dimensionless frequency of a panel structure reinforced by Al_2O_3 nanocomposite for various R/a and Al_2O_3 weight fractions.
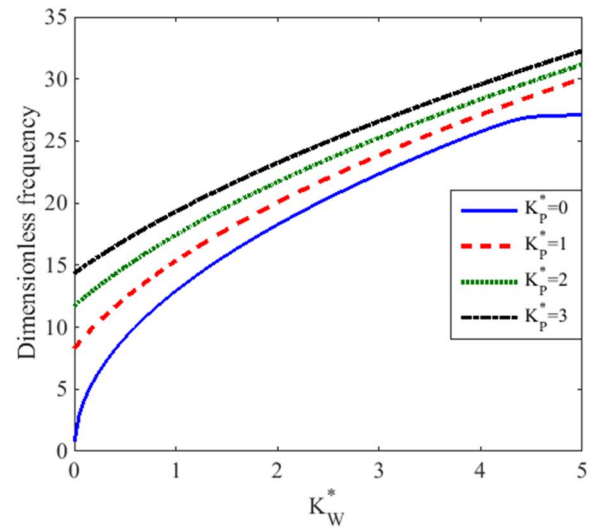
Figure 8. Dimensionless frequency of a panel structure reinforced by Al_2O_3 nanocomposite for various R/a and K_W^* ratios.

Figure 9. Dimensionless frequency of a panel structure reinforced by Al_2O_3 nanocomposite for various K_P^* and K_W^* ratios.

reinforcement. This figure effectively highlights the sensitivity of the structure's dynamic properties, particularly the frequency, to both the Al_2O_3 weight fraction and the radius of curvature factor, which are key parameters in the design and performance of reinforced concrete bridge structures.

Figure 8 presents the variation of dimensionless frequency as a function of the dimensionless Winkler coefficient, for different values of the dimensionless radius of curvature factor, R/a, in a reinforced Al_2O_3 nanocomposite concrete structure supported by an elastic foundation. The horizontal axis represents the Winkler coefficient, (ranging from 0 to 5), which models the stiffness of the elastic substrate, and the vertical axis displays the dimensionless frequency. The plot includes four curves, each representing different values of R/a, which is the ratio of the radius of curvature to the characteristic length of the structure. The blue curve corresponds to $R/a = 1$, the red dashed curve to $R/a = 2$, the green dotted curve to $R/a = 3$, and the black dashed curve to $R_x/a = 4$. As the Winkler coefficient increases, the dimensionless frequency also increases across all values of R/a. The highest frequency values are observed for $R/a = 1$, indicating that more curved structures (with a lower radius of curvature) exhibit a greater sensitivity to changes in the Winkler foundation stiffness. On the other hand, the frequency response for flatter structures (higher R/a is less pronounced but still exhibits an upward trend with increasing K_W^*. The influence of the Winkler coefficient becomes more significant as K_W^* increases, which implies that the interaction between the structure and its elastic foundation plays a key role in determining the overall frequency behavior, especially for more curved surfaces. This figure demonstrates the critical impact of the Winkler coefficient on the dynamic characteristics of curved Al_2O_3-reinforced concrete structures.

Figure 9 presents a plot showcasing the relationship between the dimensionless Winkler coefficient and the dimensionless frequency of a curved surface structure. This structure consists of an Al_2O_3 nanocomposite reinforced bridge concrete material, surrounded by an elastic substrate.
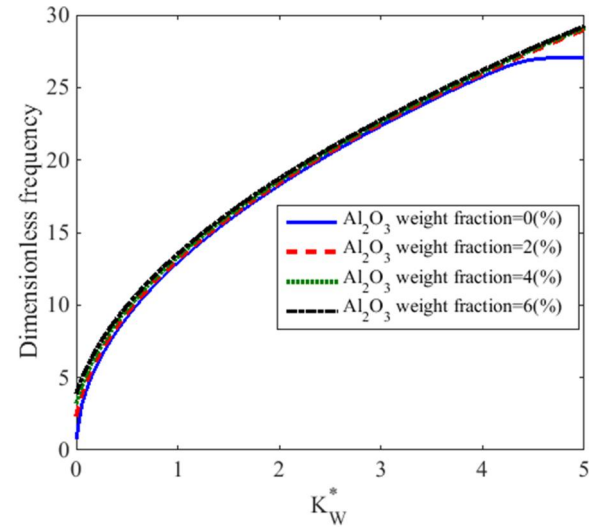
Figure 10. Dimensionless frequency of a panel structure reinforced by Al_2O_3 nanocomposite for various K_W^* and Al_2O_3 weight fractions.

The plot highlights how the dimensionless frequency varies for different values of the dimensionless Pasternak coefficient K_P^* under a range of K_W^* values. In this context, the parameter R/a denotes the dimensionless radius curvature factor, representing the curvature effect of the structure, while a/h refers to the length-to-thickness ratio, capturing the geometry of the curved surface. As K_W^* increases along the x-axis, the dimensionless frequency grows for all values of K_P^*, reflecting how the elastic foundation's stiffness affects the system's vibrational characteristics. The sensitivity of frequency to the radius curvature factor (RFC) is also influenced by the increasing values of K_P^*, as depicted by the different curves. The blue solid line represents $K_P^* = 0$, corresponding to no Pasternak foundation influence, while the dashed lines (red, green, and black) represent increasing values of $K_P^* = 1, 2, 3$, respectively. As K_P^* rises, the dimensionless frequency increases for a given K_W^*, indicating that both the Winkler and Pasternak parameters play a significant role in enhancing the stiffness of the elastic foundation, thus

raising the natural frequencies of the nanocomposite structure. The plot offers insight into how the elastic substrate parameters affect the vibrational response of bridge concrete nanocomposite structures with varying curvature.

Figure 10 illustrates the variation in the dimensionless frequency with respect to the dimensionless Winkler coefficient K_W^* for different weight fractions of Al_2O_3 in a nanocomposite material used in bridge concrete structures. The plot shows four curves, each corresponding to a different Al_2O_3 weight fraction: 0%, 2%, 4%, and 6%. On the x-axis, the dimensionless Winkler coefficient represents the stiffness of the elastic foundation, while the y-axis shows the dimensionless frequency. As K_W^* increases, the dimensionless frequency increases for all Al_2O_3 weight fractions, indicating that the elastic foundation contributes significantly to the vibrational behavior of the structure. The blue solid line represents the case where the Al_2O_3 weight fraction is 0%, while the dashed lines (red, green, and black) represent increasing weight fractions of 2%, 4%, and 6%, respectively. As the weight fraction of Al_2O_3 increases, the dimensionless frequency shows a slight increase, particularly at higher values of K_W^*. This suggests that the inclusion of Al_2O_3 in the composite material enhances its stiffness and contributes to higher natural frequencies. The plot demonstrates that the Al_2O_3 weight fraction has a minor but noticeable effect on the overall frequency behavior, with higher weight fractions resulting in slightly stiffer structures. However, the curves are relatively close to each other, indicating that the influence of Al_2O_3 weight fraction on frequency becomes more prominent at higher values of the Winkler coefficient. This analysis is important for understanding the role of material composition in the dynamic performance of bridge structures.

Figure 11 shows the relationship between the length-to-thickness ratio and the sensitivity of frequency to the radius curvature factor for different weight fractions of Al_2O_3 (aluminum oxide) in a composite material. The RFC represents the sensitivity of the structure's frequency to changes in its curvature, and a/h describes the geometry of
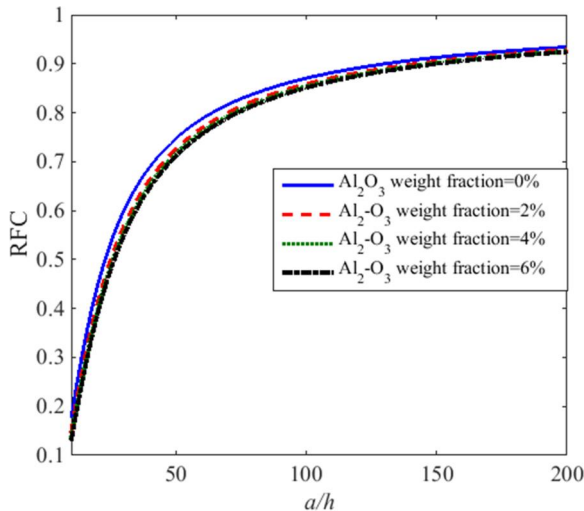
the structure, with larger values of a/h corresponding to thinner structures. The x-axis represents the length-to-thickness ratio, while the y-axis shows the RFC. Four curves are plotted, each representing a different Al_2O_3 weight fraction: 0%, 2%, 4%, and 6%. The blue solid line corresponds to an Al_2O_3 weight fraction of 0%, while the red dashed, green dotted, and black dash-dotted lines represent weight fractions of 2%, 4%, and 6%, respectively. As a/h increases, the RFC increases for all weight fractions, indicating that thinner structures are more sensitive to curvature effects on their natural frequency. At smaller values of a/h, there is a more significant difference between the curves, but as a/h increases, the curves converge, showing that the effect of Al_2O_3 weight fraction becomes less pronounced in thinner structures. For larger a/h values (beyond 150), all curves tend toward an RFC of approximately 0.9, meaning the sensitivity of frequency to curvature reaches a near-constant level. The figure demonstrates that increasing the Al_2O_3 weight fraction slightly enhances the RFC at lower a/h ratios, but the effect diminishes as the structure becomes thinner. This behavior highlights the influence of material composition on the dynamic sensitivity of bridge concrete structures to curvature changes, particularly in thicker configurations.

Figure 12 presents a graph that illustrates the relationship between the sensitivity of frequency to the radius curvature factor (RFC) and the length-to-thickness ratio for various dimensionless Winkler coefficients. The graph specifically focuses on the behavior of a curved surface structure composed of an Al_2O_3 nanocomposite-reinforced bridge concrete, which is surrounded by an elastic substrate. The horizontal axis represents the length-to-thickness ratio, which ranges from 0 to 200. The vertical axis shows the RFC, which varies between 0.1 and 0.9. The different curves in the graph correspond to various values of the dimensionless Winkler coefficient, including $K_W^* = 0$ (solid blue line), $K_W^* = 0.1$ (dashed red line), $K_W^* = 0.2$ (dotted green line), and $K_W^* = 0.3$ (dash-dotted black line). For each value of K_W^*, the graph shows how RFC increases rapidly with
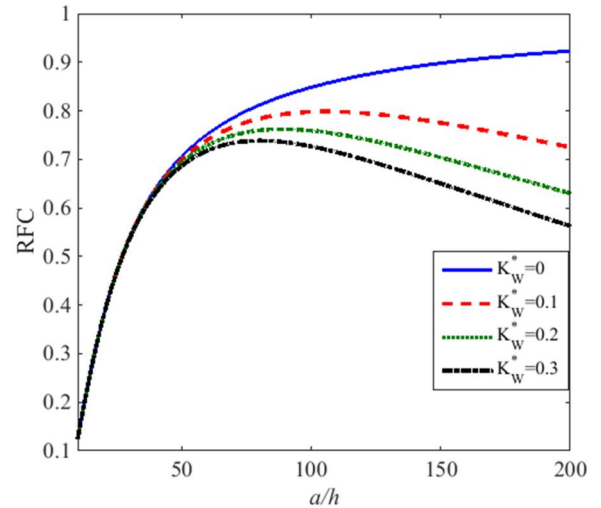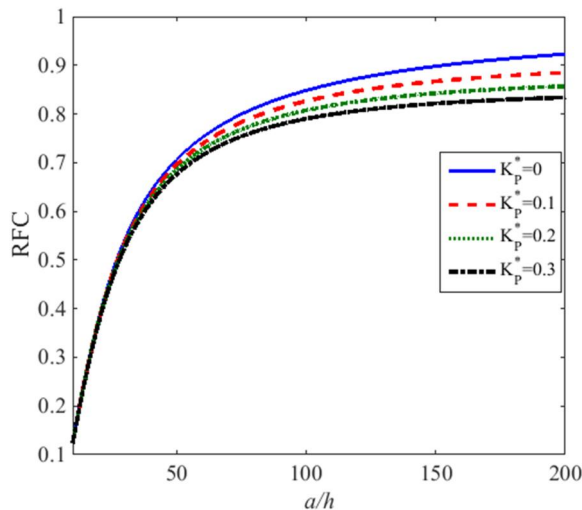

Figure 11. Sensitivity of frequency to radius curvature factor of a panel structure reinforced by Al_2O_3 nanocomposite for various Al_2O_3 weight fraction and a/h ratios.

Figure 12. Sensitivity of frequency to radius curvature factor of a panel structure reinforced by Al_2O_3 nanocomposite for various K_W^* and a/h ratios.

increasing a/h, reaching a peak at approximately $a/h = 50$, after which it gradually decreases as a/h continues to rise. The effect of increasing K_W^* is evident, as higher values of the Winkler coefficient tend to lower the RFC across the entire range of a/h, indicating that greater elastic support from the substrate (higher K_W^*) reduces the sensitivity of frequency to the radius curvature factor. In summary, the graph captures the interaction between the structural parameters of the Al_2O_3 composite bridge concrete and the elastic foundation, highlighting the influence of the elastic substrate on the frequency response of the system.

Figure 13 illustrates the relationship between the sensitivity of frequency to the radius curvature factor and the length-to-thickness ratio for different values of the dimensionless Pasternak coefficient. The graph represents a curved surface structure made of Al_2O_3 nanocomposite-reinforced bridge concrete, which is surrounded by an elastic substrate. The horizontal axis represents the length-to-thickness ratio, which spans values from 0 to 200. The vertical axis shows RFC values, ranging from 0.1 to 0.9. The graph contains four curves, each corresponding to a specific value of the Pasternak coefficient K_P^*: $K_P^* = 0$ (solid blue line), $K_P^* = 0.1$ (dashed red line), $K_P^* = 0.2$ (dotted green line), and $K_P^* = 0.3$ (dash-dotted black line). As observed in the graph, for all values of K_P^*, the RFC increases rapidly with increasing a/h, reaching a maximum value around $a/h = 50$, and then gradually stabilizing. The effect of the Pasternak coefficient is evident, as larger values of K_P^* result in lower RFC values throughout the entire range of a/h. This suggests that increasing the Pasternak coefficient, which accounts for shear interaction in the elastic foundation, reduces the frequency sensitivity to the radius curvature factor. Overall, the figure demonstrates that higher Pasternak coefficients lead to a less pronounced sensitivity of frequency to curvature, indicating that shear effects in the elastic substrate play a significant role in the structural dynamics of the composite bridge concrete system.

Figure 14 depicts the relationship between the sensitivity of frequency to the radius curvature factor and the length-to-thickness ratio for different values of the dimensionless radius curvature factor. The structure considered is the curved surface of an Al_2O_3 nanocomposite reinforced bridge concrete, surrounded by an elastic substrate. The horizontal axis represents the length-to-thickness ratio, which spans values from 0 to 200. The vertical axis shows RFC, which varies between 0.1 and 0.9. The graph includes four curves representing different values of the dimensionless radius curvature factor, namely $R/a = 5$ (solid blue line), $R/a = 10$ (dashed red line), $R/a = 15$ (dotted green line), and $R_x/a = 20$ (dash-dotted black line). In general, for all values of R/a, RFC increases as the length-to-thickness ratio rises, with a more significant increase observed when a/h is smaller. The curves approach a peak RFC value around $a/h = 50$, after which they level off. As R/a increases, the RFC values are generally higher for the same a/h values, indicating that larger radius curvature factors lead to greater frequency sensitivity. The behavior in the graph suggests that as the radius of curvature increases, the structure becomes more sensitive to changes in frequency, particularly for smaller length-to-thickness ratios. This implies that larger curved surfaces in the composite concrete bridge structure will experience greater frequency effects, especially in the lower range of a/h values.

7.4. Testing, training and presenting the results

The results are then given after being assessed by mathematical modeling and experimental validation. When the number of starting epochs in the training and validation sets of the loss-error curve differs, the network is said to be trained. However after a given number of epochs, the network gets overfitted and stops performing effectively with the training set, even if the training error lowers. For the validation data set and any further input data, this produces inflated and
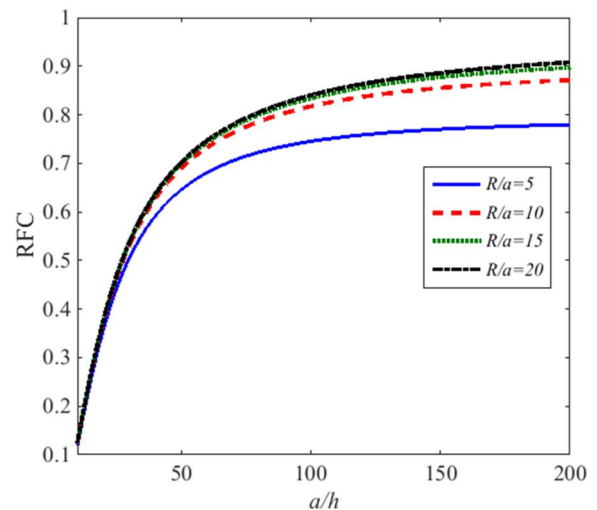

Figure 13. Sensitivity of frequency to radius curvature factor of a panel structure reinforced by Al_2O_3 nanocomposite for various K_P^* and a/h ratios.

Figure 14. Sensitivity of frequency to radius curvature factor of a panel structure reinforced by Al_2O_3 nanocomposite for various R/a and a/h ratios.

Table 2. Dimensionless frequency of the DNN model for different RMSE and a/h values.

a/h	MMR	Predicted		
		$RMSE_{Train} = 0.8125$	$RMSE_{Train} = 0.8951$	$RMSE_{Train} = 0.9191$
20	4.689	3.62119	4.46633	4.69493
40	3.942	3.23011	3.61439	3.94196
60	2.655	1.81374	2.31287	2.65793
80	1.701	1.41287	1.58387	1.70663
100	0.927	0.59244	0.88728	0.92659

Table 3. Performance of the DNN model for dimensionless frequency for various R^2 and weight fraction of Al_2O_3.

Weight fraction of Al_2O_3	MMR	Predicted		
		$R^2 = 0.9352$	$R^2 = 0.9631$	$R^2 = 0.9891$
0%	2.304	1.7057	2.15867	2.30924
1%	3.312	2.31287	2.83754	3.30824
2%	3.609	2.71375	3.3761	3.60858
3%	5.265	3.79424	4.48769	5.26871
4%	6.318	4.83287	6.00263	6.32269

erroneous findings. Our findings indicate that in order to guarantee consistent outcomes, at least 390 epochs are required. This big epoch size keeps the amplitude accurate and avoids overfitting. This section looks at how R^2 and RMSE affect the outcomes shown in Tables 2 and 3. Higher RMSE and R^2 values have been observed to result in more accurate replies. As a result, while choosing the results, it is advised to pick $R^2=0.9891$, RMSE = 0.9191, and 591 samples. MMR also presents the outcomes of the mathematical modeling.

Tables 2 and 3 illustrate how the dimensionless frequency of the current structure varies with the weight fraction of Al_2O_3 and a/h. This topic will be covered in more detail in the following section.

8. Conclusion

This study provided a comprehensive vibration analysis of Al2O3 nanocomposite-reinforced concrete bridge structures resting on an innovative elastic foundation using the Carrera Unified Formulation. By incorporating Al2O3 nanoparticles within the concrete matrix, significant improvements in the mechanical properties of the bridge structures were observed, particularly in terms of stiffness, damping, and overall vibrational performance. The novel elastic foundation model employed in this analysis offered a more realistic representation of soil-structure interaction, leading to more accurate predictions of dynamic behavior under various loading conditions. The results obtained through CUF were thoroughly validated using nondestructive testing methods, which delivered valuable insights into the structural integrity and vibrational response of the bridge structures. NDT proved to be a reliable tool for detecting potential damages and anomalies, thereby reinforcing the accuracy of the CUF-based predictions. Additionally, machine learning algorithms were utilized to efficiently predict vibrational characteristics, offering a valuable computational resource for structural health monitoring systems. The integration of these methodologies—CUF for high-fidelity vibration analysis, NDT for experimental validation, and ML for predictive modeling—demonstrated a robust framework for evaluating and analyzing reinforced concrete bridge structures. The findings from this study underscored the potential of Al_2O_3 nanocomposites to enhance the vibrational performance of concrete structures, leading to improved resilience and an extended lifespan. Moreover, the innovative elastic foundation model introduced in this research offered practical solutions for optimizing foundation design, particularly for bridges subjected to complex environmental and load conditions. Future research was suggested to explore the application of these methodologies to other structural configurations, materials, and foundation models, to further validate their effectiveness. The combination of CUF, NDT, and ML promised to advance the field of structural engineering, enabling more accurate, efficient, and reliable design and analysis of critical infrastructure. This study laid a strong foundation for continued exploration of nanocomposite reinforcement in civil engineering and contributed to the growing body of knowledge in vibration analysis and structural health monitoring.

Disclosure statement

Funding

References

[1] E. Mohseni, A.R. Saidi and M. Mohammadi, Bending-stretching analysis of thick functionally graded micro-plates using higher-order shear and normal deformable plate theory, Mech. Adv. Mater. Struct., vol. 24, no. 14, pp. 1221–1230, 2017. DOI: 10.1080/15376494.2016.1227503.

[2] Z.-Z. Wang, T. Wang, Y-m Ding and L-s Ma, A simple refined plate theory for the analysis of bending, buckling and free vibration of functionally graded porous plates reinforced by graphene platelets, Mech. Adv. Mater. Struct., vol. 31, no. 8, pp. 1699–1716, 2024. DOI: 10.1080/15376494.2022.2141383.

[3] H.-S. Shen, X.-H. Huang and J. Yang, Nonlinear bending of temperature-dependent FG-CNTRC laminated plates with negative poisson's ratio, Mech. Adv. Mater. Struct., vol. 27, no. 13, pp. 1141–1153, 2020. DOI: 10.1080/15376494.2020.1716412.

[4] A.G. Chanda and D. Punera, Porosity-dependent free vibration and transient responses of functionally graded composite plates employing higher order thickness stretching model, Mech. Adv. Mater. Struct., vol. 31, no. 7, pp. 1491–1516, 2024. DOI: 10.1080/15376494.2022.2138652.

[5] C. Lin, G. Pan and M. Abbas, Introducing ANN-GP algorithm to estimate transient bending of the functionally graded graphene origami-enabled auxetic metamaterial structures, Mech. Adv. Mater. Struct., pp. 1–20, 2024. DOI: 10.1080/15376494.2024.2344020.

[6] J. Najd, E. Zappino, E. Carrera, W. Harizi and Z. Aboura, Optimal position and dimensions of embedded normal

piezoelectric transducers, higher order plate models and experimental approach, Mech. Adv. Mater. Struct., pp. 1–12, 2024. DOI: 10.1080/15376494.2024.2342028.

[7] E. Carrera and V.V. Zozulya, Carrera unified formulation (CUF) for the shells of revolution. Numerical evaluation, Mech. Adv. Mater. Struct., vol. 31, no. 7, pp. 1597–1619, 2024. DOI: 10.1080/15376494.2022.2140234.

[8] E. Carrera, Theories and finite elements for multilayered plates and shells: a unified compact formulation with numerical assessment and benchmarking, ARCO., vol. 10, no. 3, pp. 215–296, 2003. DOI: 10.1007/BF02736224.

[9] A.M.A. Neves, A.J.M. Ferreira, E. Carrera, M. Cinefra, R.M.N. Jorge and C.M.M. Soares, Buckling analysis of sandwich plates with functionally graded skins using a new quasi-3D hyperbolic sine shear deformation theory and collocation with radial basis functions, Z Angew. Math. Mech., vol. 92, no. 9, pp. 749–766, 2012. DOI: 10.1002/zamm.201100186.

[10] Z. Zhong, S. Chen and E. Shang, Analytical solution of a functionally graded plate in cylindrical bending, Mech. Adv. Mater. Struct., vol. 17, no. 8, pp. 595–602, 2010. DOI: 10.1080/15376494.2010.517729.

[11] A. Belounar, S. Benmebarek and L. Belounar, Strain based triangular finite element for plate bending analysis, Mech. Adv. Mater. Struct., vol. 27, no. 8, pp. 620–632, 2020. DOI: 10.1080/15376494.2018.1488310.

[12] S.-R. Li, F. Zhang and R.-G. Liu, Classical and homogenized expressions for the bending solutions of FGM plates based on the four variable plate theories, Mech. Adv. Mater. Struct., vol. 31, no. 15, pp. 3413–3424, 2023. DOI: 10.1080/15376494.2023.2177909.

[13] K. Bendine, F.B. Boukhoulda, B. Haddag and M. Nouari, Active vibration control of composite plate with optimal placement of piezoelectric patches, Mech. Adv. Mater. Struct., vol. 26, no. 4, pp. 341–349, 2019. DOI: 10.1080/15376494.2017.1387324.

[14] M. Burkov and A. Eremin, Evaluation of fracture toughness of hybrid CNT/CFRP composites, Mech. Adv. Mater. Struct., vol. 30, no. 14, pp. 2872–2881, 2023. DOI: 10.1080/15376494.2022.2064569.

[15] R. Augello, A. Pagani and E. Carrera, Analysis of plate reinforced by straight and curved stiffeners by using novel plate elements with refined through-the-thickness expansion, Mech. Adv. Mater. Struct., pp. 1–4, 2023. DOI: 10.1080/15376494.2023.2270794.

[16] E. Carrera, F. Miglioretti and M. Petrolo, Accuracy of refined finite elements for laminated plate analysis, Compos. Struct., vol. 93, no. 5, pp. 1311–1327, 2011. DOI: 10.1016/j.compstruct.2010.11.007.

[17] E. Carrera, M. Didem Demirbas and R. Augello, Evaluation of stress distribution of isotropic, composite, and FG beams with different geometries in nonlinear regime via carrera-unified formulation and lagrange polynomial expansions, Appl. Sci., vol. 11, no. 22, pp. 10627, 2021. DOI: 10.3390/app112210627.

[18] F. Boumediene, E.M. Daya, J.-M. Cadou and L. Duigou, Forced harmonic response of viscoelastic sandwich beams by a reduction method, Mech. Adv. Mater. Struct., vol. 23, no. 11, pp. 1290–1299, 2016. DOI: 10.1080/15376494.2015.1068408.

[19] E. Carrera, Transverse normal strain effect on thermal stress analysis of homogeneous and layered plates, AIAA J., vol. 43, no. 10, pp. 2232–2242, 2005. DOI: 10.2514/1.11230.

[20] D. Hu, H. Sun, P. Mehrabi, Y.A. Ali and M. Al-Razgan, Application of artificial intelligence technique in optimization and prediction of the stability of the walls against wind loads in building design, Mech. Adv. Mater. Struct., vol. 31, no. 19, pp. 4755–4772, 2023. DOI: 10.1080/15376494.2023.2206208.

[21] J. Wu, Y. Yang, P. Mehrabi and E.A. Nasr, Efficient machine-learning algorithm applied to predict the transient shock reaction of the elastic structure partially rested on the viscoelastic substrate, Mech. Adv. Mater. Struct., vol. 31, no. 16, pp. 3700–3724, 2023. DOI: 10.1080/15376494.2023.2183289.

[22] E. Carrera, Mixed layer-wise models for multilayered plates analysis, Compos. Struct., vol. 43, no. 1, pp. 57–70, 1998. DOI: 10.1016/S0263-8223(98)00097-X.

[23] E. Carrera, A class of two-dimensional theories for anisotropic multilayered plates analysis, Atti Della Accademia Delle Scienze Di Torino. Classe Di Scienze Fisiche Matematiche e Naturali., vol. 19, pp. 1–39, 1995.

[24] M.H. Amini, M. Soleimani, A. Altafi and A. Rastgoo, Effects of geometric nonlinearity on free and forced vibration analysis of moderately thick annular functionally graded plate, Mech. Adv. Mater. Struct., vol. 20, no. 9, pp. 709–720, 2013. DOI: 10.1080/15376494.2012.676711.

[25] A. Robaldo, E. Carrera and A. Benjeddou, A unified formulation for finite element analysis of piezoelectric adaptive plates, Comput. Struct., vol. 84, no. 22–23, pp. 1494–1505, 2006. DOI: 10.1016/j.compstruc.2006.01.029.

[26] E. Carrera, Developments, ideas, and evaluations based upon Reissner's mixed variational theorem in the modeling of multilayered plates and shells, Appl. Mech. Rev., vol. 54, no. 4, pp. 301–329, 2001. DOI: 10.1115/1.1385512.

[27] E. Carrera, Historical review of zig-zag theories for multilayered plates and shells, Appl. Mech. Rev., vol. 56, no. 3, pp. 287–308, 2003. DOI: 10.1115/1.1557614.

[28] E. Carrera and V.V. Zozulya, Carrera unified formulation (CUF) for the micropolar plates and shells. I. Higher order theory, Mech. Adv. Mater. Struct., vol. 29, no. 6, pp. 773–795, 2022. DOI: 10.1080/15376494.2020.1793241.

[29] E. Carrera and V.V. Zozulya, Carrera unified formulation for the micropolar plates, Mech. Adv. Mater. Struct., vol. 29, no. 22, pp. 3163–3186, 2022. DOI: 10.1080/15376494.2021.1889726.

[30] E. Carrera and V.V. Zozulya, Carrera unified formulation (CUF) for the composite plates and shells of revolution. layerwise models, Compos. Struct., vol. 334, pp. 117936, 2024. DOI: 10.1016/j.compstruct.2024.117936.

[31] V.V. Zozulya, and E. Carrera, Carrera unified formulation (CUF) for the micropolar plates and shells. III. Classical models, Mech. Adv. Mater. Struct., vol. 29, no. 27, pp. 6336–6360, 2022. DOI: 10.1080/15376494.2021.1975855.

[32] E. Carrera and V.V. Zozulya, Carrera unified formulation (CUF) for the composite shells of revolution. Equivalent single layer models, Mech. Adv. Mater. Struct., vol. 31, no. 1, pp. 22–44, 2024. DOI: 10.1080/15376494.2023.2218380.

[33] M. Li, T. Wang, F. Chu, Q. Han, Z. Qin and M.J. Zuo, Scaling-basis chirplet transform, IEEE Trans. Ind. Electron., vol. 68, no. 9, pp. 8777–8788, 2021. DOI: 10.1109/TIE.2020.3013537.

[34] D. Lu, J. Liang, X. Du, C. Ma and Z. Gao, Fractional elastoplastic constitutive model for soils based on a novel 3D fractional plastic flow rule, Comput. Geotech., vol. 105, pp. 277–290, 2019. DOI: 10.1016/j.compgeo.2018.10.004.

[35] D. Lu, F. Meng, X. Zhou, Y. Zhuo, Z. Gao and X. Du, A dynamic elastoplastic model of concrete based on a modeling method with environmental factors as constitutive variables, J. Eng. Mech., vol. 149, no. 12, pp. 04023102, 2023. DOI: 10.1061/JENMDT.EMENG-7206.

[36] X. Zhou, D. Lu, X. Du, G. Wang and F. Meng, A 3D non-orthogonal plastic damage model for concrete, Comput. Methods Appl. Mech. Eng., vol. 360, pp. 112716, 2020. DOI: 10.1016/j.cma.2019.112716.

[37] J. Cao, J. Du, H. Zhang, H. He, C. Bao and Y. Liu, Mechanical properties of multi-bolted glulam connection with slotted-in steel plates, Constr. Build. Mater., vol. 433, pp. 136608, 2024. DOI: 10.1016/j.conbuildmat.2024.136608.

[38] X. Long, Z. Shen, J. Li, R. Dong, M. Liu, Y. Su and C. Chen, Size effect of nickel-based single crystal superalloy revealed by nanoindentation with low strain rates, J. Mater. Res. Technol., vol. 29, pp. 2437–2447, 2024. DOI: 10.1016/j.jmrt.2024.01.279.

[39] Y. Wang and O. Sigmund, Multi-material topology optimization for maximizing structural stability under thermo-mechanical loading, Comput. Methods Appl. Mech. Eng., vol. 407, pp. 115938, 2023. DOI: 10.1016/j.cma.2023.115938.

[40] J. Wang, S.-Q. Lin, D.-Y. Tan, J.-H. Yin, H.-H. Zhu and S.C. Kuok, A novel method for integrity assessment of soil-nailing works with actively heated fiber-optic sensors, J. Geotech. Geoenviron. Eng., vol. 150, no. 8, pp. 04024063, 2024. DOI: 10.1061/JGGEFK.GTENG-11790.

[41] H. Khorshidi, C. Zhang, E. Najafi and M. Ghasemi, Fresh, mechanical and microstructural properties of alkali-activated composites incorporating nanomaterials: a comprehensive review, J. Cleaner Prod., vol. 384, pp. 135390, 2022. DOI: 10.1016/j.jclepro.2022.135390.

[42] B. Liu, H. Yang and S. Karekal, Effect of water content on argillization of mudstone during the tunnelling process, Rock Mech. Rock Eng., vol. 53, no. 2, pp. 799–813, 2020. DOI: 10.1007/s00603-019-01947-w.

[43] H. Yang, C. Chen, J. Ni and S. Karekal, A hyperspectral evaluation approach for quantifying salt-induced weathering of sandstone, Sci. Total Environ., vol. 885, pp. 163886, 2023. DOI: 10.1016/j.scitotenv.2023.163886.

[44] H. Yang, K. Song and J. Zhou, Automated recognition model of geomechanical information based on operational data of tunneling boring machines, Rock Mech. Rock Eng., vol. 55, no. 3, pp. 1499–1516, 2022. DOI: 10.1007/s00603-021-02723-5.

[45] C. Chen, H. Yang, K. Song, D. Liang, Y. Zhang and J. Ni, Dissolution feature differences of carbonate rock within hydro-fluctuation belt located in the three gorges reservoir area, Eng. Geol., vol. 327, pp. 107362, 2023. DOI: 10.1016/j.enggeo.2023.107362.

[46] H. Yang, J. Ni, C. Chen and Y. Chen, Weathering assessment approach for building sandstone using hyperspectral imaging technique, Herit. Sci., vol. 11, no. 1, pp. 70, 2023. DOI: 10.1186/s40494-023-00914-7.

[47] K. Song, H. Yang, D. Liang, L. Chen and M. Jaboyedoff, Step-like displacement prediction and failure mechanism analysis of slow-moving reservoir landslide, J. Hydrol., vol. 628, pp. 130588, 2024. DOI: 10.1016/j.jhydrol.2023.130588.

[48] S. Han, D. Zheng, B. Mehdizadeh, E.A. Nasr, M.U. Khandaker, M. Salman and P. Mehrabi, Sustainable design of self-consolidating green concrete with partial replacements for cement through neural-network and fuzzy technique, Sustainability., vol. 15, no. 6, pp. 4752, 2023. DOI: 10.3390/su15064752.

[49] S. Han, Z. Zhu, M. Mortazavi, A.M. El-Sherbeeny and P. Mehrabi, Analytical assessment of the structural behavior of a specific composite floor system at elevated temperatures using a newly developed hybrid intelligence method, Buildings., vol. 13, no. 3, pp. 799, 2023. DOI: 10.3390/buildings13030799.

[50] E. Taheri, P. Mehrabi, S. Rafiei and B. Samali, Numerical evaluation of the upright columns with partial reinforcement along with the utilisation of neural networks with combining feature-selection method to predict the load and displacement, Appl. Sci., vol. 11, no. 22, pp. 11056, 2021. DOI: 10.3390/app112211056.

[51] J. Liu, M. Mohammadi, Y. Zhan, P. Zheng, M. Rashidi and P. Mehrabi, Utilizing artificial intelligence to predict the superplasticizer demand of self-consolidating concrete incorporating pumice, slag, and fly ash powders, Materials., vol. 14, no. 22, pp. 6792, 2021. DOI: 10.3390/ma14226792.

[52] E. Taheri, A. Firouzianhaji, P. Mehrabi, B. Vosough Hosseini and B. Samali, Experimental and numerical investigation of a method for strengthening cold-formed steel profiles in bending, Appl. Sci., vol. 10, no. 11, pp. 3855, 2020. DOI: 10.3390/app10113855.

[53] Y. Feng, M. Mohammadi, L. Wang, M. Rashidi and P. Mehrabi, Application of artificial intelligence to evaluate the fresh properties of self-consolidating concrete, Materials., vol. 14, no. 17, pp. 4885, 2021. DOI: 10.3390/ma14174885.

[54] A. Firouzianhaji, N. Usefi, B. Samali and P. Mehrabi, Shake table testing of standard cold-formed steel storage rack, Applied

[55] Sciences., vol. 11, no. 4, pp. 1821, 2021. DOI: 10.3390/app11041821.

[55] P. Mehrabi, S. Honarbari, S. Rafiei, S. Jahandari and M. Alizadeh Bidgoli, Seismic response prediction of FRC rectangular columns using intelligent fuzzy-based hybrid metaheuristic techniques, J. Ambient Intell. Humaniz. Comput., vol. 12, no. 11, pp. 10105–10123, 2021. DOI: 10.1007/s12652-020-02776-4.

[56] P. Mehrabi, M. Shariati, K. Kabirifar, M. Jarrah, H. Rasekh, N.T. Trung, A. Shariati and S. Jahandari, Effect of pumice powder and nano-clay on the strength and permeability of fiber-reinforced pervious concrete incorporating recycled concrete aggregate, Constr. Build. Mater., vol. 287, pp. 122652, 2021. DOI: 10.1016/j.conbuildmat.2021.122652.

[57] E. Taheri, A. Firouzianhaji, N. Usefi, P. Mehrabi, H. Ronagh and B. Samali, Investigation of a method for strengthening perforated cold-formed steel profiles under compression loads, Appl. Sci., vol. 9, no. 23, pp. 5085, 2019. DOI: 10.3390/app9235085.

[58] A. Toghroli, P. Mehrabi, M. Shariati, N.T. Trung, S. Jahandari and H. Rasekh, Evaluating the use of recycled concrete aggregate and pozzolanic additives in fiber-reinforced pervious concrete with industrial and recycled fibers, Constr. Build. Mater., vol. 252, pp. 118997, 2020. DOI: 10.1016/j.conbuildmat.2020.118997.

[59] H. SafarPour and M. Ghadiri, Critical rotational speed, critical velocity of fluid flow and free vibration analysis of a spinning SWCNT conveying viscous fluid, Microfluid. Nanofluid., vol. 21, no. 2, pp. 1–23, 2017. DOI: 10.1007/s10404-017-1858-y.

[60] M. Safarpour, A. Rahimi, A. Alibeigloo, H. Bisheh and A. Forooghi, Parametric study of three-dimensional bending and frequency of FG-GPLRC porous circular and annular plates on different boundary conditions, Mech. Based Des. Struct. Mach., vol. 49, no. 5, pp. 707–737, 2021. DOI: 10.1080/15397734.2019.1701491.

[61] K. Rashvand, A. Alibeigloo and M. Safarpour, Free vibration and instability analysis of a viscoelastic micro-shell conveying viscous fluid based on modified couple stress theory in thermal environment, Mech. Based Des. Struct. Mach., vol. 50, no. 4, pp. 1198–1236, 2022. DOI: 10.1080/15397734.2020.1745079.

[62] M. Shaat, Effects of grain size and microstructure rigid rotations on the bending behavior of nanocrystalline material beams, Int. J. Mech. Sci., vol. 94–95, pp. 27–35, 2015. DOI: 10.1016/j.ijmecsci.2015.02.008.

[63] M. Shaat, A. Fathy and A. Wagih, Correlation between grain boundary evolution and mechanical properties of ultrafine-grained metals, Mech. Mater., vol. 143, pp. 103321, 2020. DOI: 10.1016/j.mechmat.2020.103321.

[64] P.S. Branicio, J.Y. Zhang and D.J. Srolovitz, Effect of strain on the stacking fault energy of copper: a first-principles study, Phys. Rev. B., vol. 88, no. 6, pp. 064104, 2013. DOI: 10.1103/PhysRevB.88.064104.

[65] M.H.G. Rad and S.M. Hosseini, The modified CUF-EFG method for the dynamic analysis of GPLs-CNTs-reinforced FG multilayer thick cylindrical shells under shock loadings: a modified meshless implementation, Eng. Anal. Bound. Elem., vol. 156, pp. 499–518, 2023. DOI: 10.1016/j.enganabound.2023.08.023.

[66] A.B. Rad, Static analysis of non-uniform 2D functionally graded auxetic-porous circular plates interacting with the gradient elastic foundations involving friction force, Aerosp. Sci. Technol., vol. 76, pp. 315–339, 2018.

[67] M.D. Olson and G.M. Lindberg, Dynamic analysis of shallow shells with a doubly-curved triangular finite element, J. Sound Vib., vol. 19, no. 3, pp. 299–318, 1971. DOI: 10.1016/0022-460X(71)90691-2.